JOURNAL OF GEOPHYSICAL RESEARCH, VOL. 103, NO. A5, PAGES 9449-9471, MAY 1, 1998

Spatial structure in the thermospheric horizontal wind above Poker Flat, Alaska, during solar minimum

M. Conde and R. W. Smith
Geophysical Institute, University of Alaska Fairbanks

Abstract. A new all-sky imaging, wavelength scanning Fabry-Perot spectrometer was used to record high-resolution ($R \simeq 200,000$) spectra of the $\lambda 630$ nm thermospheric optical emission above Poker Flat, Alaska. These spectra were used to derive spatially resolved maps of the horizontal wind vector at approximately 250 km altitude. We describe the procedure used to infer vector winds from line-of-sight Doppler shifts, along with its limitations. We present the time evolution of the vector wind fields obtained from this method for 6 nights of observation. Five of the 6 nights contained periods when we inferred the existence of significant curvature, divergence or shear in the thermospheric wind across our instrument's $\sim$1000 km diameter field of view. The sixth night exhibited little spatial structure and is shown for comparison. We compare these results with a "generic" solar minimum winter time run of the National Center for Atmospheric Research's Thermosphere, Ionosphere, and Electrodynamics General Circulation Model. While agreement was good at the start and end of the night, considerable differences were found in the late evening and midnight sectors. Some possible origins for these discrepancies are proposed. In particular, we suggest that the F region horizontal wind may be deflected by upwelling vertical winds, which are in turn driven by E region heating in the auroral zone. We note that both the instrument used and our high-latitude implementation of the analysis procedure are new experimental techniques. Thus the data presented here should be regarded as preliminary and, if possible, be validated by comparison with results from other techniques.

1. Introduction

Previous accounts of thermospheric dynamics have highlighted processes which remove complexity from thermospheric wind systems [e.g., *Killeen and Roble*, 1988; *Killeen et al.*, 1988; *Smith et al.*, 1988]. In particular, viscosity is known to oppose both horizontal and vertical velocity shears, so it is tempting to presume that thermospheric wind fields should appear smooth and laminar at smaller than synoptic spatial scales. However, many existing observational and theoretical studies suggest this is not necessarily the case and that significant structure actually can appear in thermospheric winds at spatial scales of several hundred kilometers, or less. The purpose of the experimental study presented here was to attempt to observe such structure.

Previous studies of neutral wind data have shown strong velocity shears in the horizontal wind at high latitude [e.g., *Spencer et al.*, 1982; *Hays et al.*, 1984; *Killeen et al.*, 1988]. The global-scale relationship between thermospheric winds and auroral morphology has been examined by *Killeen et al.* [1988]. A principal outcome of this study was to demonstrate the close association between reversals and boundaries in the neutral wind and the location of the aurora. Theoretical atmospheric models also predict that strong shears may develop in the thermospheric wind field within several hundred kilometers of an auroral arc [*St. Maurice and Schunk*, 1981; *Fuller-Rowell*, 1985; *Lyons and Walterscheid*, 1985; *Walterscheid et al.*, 1985; *Chang and St.-Maurice*, 1991; *Walterscheid and Lyons*, 1992; *Keskinen and Satyanarayana*, 1993].

Ground-based Fabry-Perot spectrometers (FPS) have been measuring thermospheric winds in the auroral zone for many years, although they have typically been limited to observing in only four azimuths. Nevertheless, we may expect evidence of small-scale wind structures, if they exist, to appear in the FPS records in the form of differences in the line-of-sight wind components seen when viewing in opposite azimuths. In practice, differences like this actually do appear very commonly in the high-latitude FPS data. A good example from the literature is given by *Smith et al.* [1994, Figure 5]. As well as obvious large-scale differences between the observations and model predictions, their observed winds show small-scale structure with amplitudes well in excess of the measurement error of around 10 $\mathrm{m\,s^{-1}}$.

Paper number 97JA03331
0148-0227/48/97JA-03331 $09.00.

This structure appears both as temporal scatter in the wind values observed in each viewing direction and as systematic differences between the line-of-sight components obtained when viewing in azimuthally opposite directions. The latter effect indicates spatial structure over length scales comparable to the separation of viewing fields (about 800 km) whereas the former presumably arises from smaller scale features.

Although not directly measuring horizontal structure, zenith-only FPS observations yield estimates of the thermospheric vertical wind and overhead temperature. These data and their spatial association with the aurora are also suggestive of horizontal structure on spatial scales of several hundred kilometers [see, for example, *Rees et al.*, 1984b; *Wardill and Jacka*, 1986; *Crickmore et al.*, 1991; *Price and Jacka*, 1991; *Price et al.*, 1995; *Innis et al.* 1996]. These studies appear to suggest that downward winds occur near the equatorward edge of the auroral oval, whereas upwelling occurs on the poleward edge of the oval. The Price et al. and Innis et al. studies both yielded estimates of the size of the upwelling region of around 400 km, at least in the latitudinal direction.

The observations reported here were obtained during wintertime solar minimum conditions using a Fabry-Perot spectrometer located at Poker Flat, Alaska. The wind measurements were derived from Doppler shifts of the λ630 nm optical emission from atomic oxygen, originating at $\sim$ 240 km altitude. Thermospheric winds have been measured in this location previously using ground-based Fabry-Perot spectrometers [*Nagy et al.*, 1974; *Hays et al.*, 1979; *Sica et al.*, 1986, 1989, 1993; *Smith et al.*, 1989], rocket-borne chemical releases [*Meriwether et al.*, 1973; *Mikkelsen et al.*, 1981; *Heppner and Miller*, 1982; *Larsen et al.*, 1995, 1997], incoherent scatter radar [*Bates and Roberts*, 1977; *Wickwar et al.*, 1984] and by the Dynamics Explorer 2 satellite [e.g., *Killeen and Roble*, 1988].

With the exception of the DE 2 satellite, these measurements have returned little detailed information about the spatial variation of the horizontal wind field. Rocket flights can measure the wind in two locations that are up to several hundred kilometers apart using upleg and downleg chemical releases, and in March 1970 there were two experiments involving pairs of rockets launched simultaneously from Alaska about 550 km apart [*Meriwether et al.*, 1973]. A ground-based Fabry-Perot spectrometer only needs three independent viewing directions to estimate all three components of the uniform wind field. Since a typical observing scheme involves viewing in four azimuths plus directly in the zenith, there is some redundant information from which to estimate nonuniformity. However, neither the chemical releases nor the five-direction Fabry-Perot interferometer experiments can provide enough information to uniquely estimate all of the terms required to describe even first-order departures from a uniform horizontal wind vector field.

The Dynamics Explorer 2 satellite was able to measure spatial variations of the wind vector along the satellite track. Nevertheless, these data still only describe wind variations with respect to one spatial dimension (i.e., along track), and the spatial resolution for the meridional wind data was limited to typically $\sim$500 km by the satellite's limb viewing geometry [*Killeen and Roble*, 1988]. A further problem with all such spacecraft measurements is that they are obtained as snapshots in time, during individual satellite overpasses. It is not possible to follow the time evolution of a particular flow configuration in the wind field.

2. Instrument Description

The measurements reported here were obtained with a new type of all-sky imaging Fabry-Perot spectrometer (ASI-FPS). Several ASI-FPS instruments have been described previously [*Rees and Greenaway*, 1983; *Rees et al.*, 1984a; *Sekar et al.*, 1993; *Biondi et al.*, 1995; *Nakajima et al.*, 1995; *Ishii et al.*, 1997]. These instruments are able to measure the line-of-sight component of the neutral wind at several tens of locations across the sky and thus can, in principle, estimate not only the uniform wind but also its spatial variation within the region viewed. *Batten et al.* [1988] and *Batten and Rees*, [1990] reported using such an instrument to observe thermospheric wind features varying over spatial scales of 100-300 km and over temporal scales as short as 10 min. However, the instrument used in those studies employed an etalon with a fixed plate spacing and recovered spectral information by analyzing the shapes of the interference fringes formed by the etalon. Indeed, all of the ASI-FPS instruments mentioned above operate this way.

Although this approach is reasonable at midlatitudes, *Conde and Smith* [1995, 1997] point out that it may not be suitable in the auroral zone (where most small-scale wind features would be expected to occur) because the fringe shapes are also a function of the auroral luminosity distribution. Since the aurora can contain large spatial intensity gradients, these are likely to produce artifacts in the recovered spectra which will ultimately be interpreted as small-scale perturbations to the wind field. The ASI-FPS instrument used in the present study (described by *Conde and Smith* [1997]) encodes spectral information by scanning the etalon plate spacing over time. Because the etalon scan is independent of the spatial distribution of luminosity, this instrument is unaffected by spatial intensity gradients. Because the etalon scan is time-varying, there is a potential for temporal fluctuations of source brightness to distort the inferred spectra. The instrument suppresses these distortions to an insignificant level by coadding many tens of short duration scans of the spectrum during each spectral integration.

The instrument used here is based on a 100 mm aperture capacitance-stabilized Fabry-Perot etalon, the plates of which are piezoelectrically scannable in spacing over approximately 1.5 orders of interference (at λ630 nm) about a nominal 20 mm gap. Skylight is coupled into the etalon through an all-sky lens and op-

tical relay system which maps an approximately 65° half-angle field-of-view onto 5 orders of interference at the etalon. Interference fringes formed by the etalon are conjugate with the sky. The sky, modulated by this fringe pattern, is reimaged onto an imaging photon detector (IPD) after first passing through a narrowband interference filter. The spectral distribution of incident photons is recovered using both their arrival positions on the detector and the etalon scan channel prevailing at the detection time. As mentioned, this procedure is quite different from that of previous fixed-etalon ASI-FPS instruments. A second advantage of scanning the etalon is that this instrument makes equal use of spectral information from all parts of its field of view. By contrast, a nonscanned instrument only obtains useful spectral information from narrow annular regions of its field of view, corresponding to the bright portions of the Fabry-Perot fringe pattern.

For the observations described here, the instrument was configured to measure line-of-sight winds simultaneously from 25 independent "zones," mapping onto the sky as sectors of four concentric, annular, rings centered about the zenith. The ring edges were spaced uniformly in zenith angle, with the outermost being at 65°. The rings contained 1, 4, 8 and 12 sectors, respectively.

The actual division of the total field-of-view into zones is done entirely in software. The control computer generates a two-dimensional "zone map" which stores, for each detector pixel, the number of the zone to which that pixel belongs. Whenever a photon arrival is detected at a given pixel, the zone map is consulted to determine which zone that photon will be allocated to. This allows any number and any geometric pattern of zones to be defined. The zones need not be contiguous and, if desired, the allocation of zones could even be modified during an exposure. This latter capability may be useful, for example, to follow some feature moving across the field of view.

3. Estimation of Vector Winds

3.1. Raw Data and Initial Analysis

Raw data recorded by the FPS over a night consist of a time series of "exposures," each of typically 15 min duration. Each exposure yields a separate spectrum for each of the allocated zones. Each spectrum is a vector of samples of the emission's spectral distribution, convolved with the spectrometer's instrument function [*Wilksch*, 1985], and spans a wavelength interval equal to one free spectral range of the Fabry-Perot etalon. The number of samples per spectrum is configurable; typically, 128 samples are taken.

The first step in data reduction is to fit model emission spectra to the recorded spectra, allowing for broadening due to the instrument function. The calibrations and mathematical procedures required for this are described by *Conde and Smith* [1997]. The analysis returns estimates for the sample number at which the model spectrum maximizes and the width of the model spectrum in units of number of samples. Calibration data allow these estimates to be transformed to wavelength units. Temperatures may then be calculated directly from the emission spectral widths.

The line-of-sight velocity of the emission region in the atmosphere (relative to the observatory) can be inferred from the Doppler shifts of the emission peak wavelengths. However, this requires an estimate of the emission wavelength corresponding to a relative velocity of zero. In our current experimental procedure, these "rest wavelength" estimates are derived from the sky spectra themselves. For each sky exposure, the emission wavelength estimates from all observing zones are sorted. The two highest and two lowest values are rejected, to remove possible contamination by statistical outliers. A mean value is calculated from the remaining wavelength estimates. This returns a time series of mean wavelengths (with one value for each exposure) which is then three-point smoothed. The smoothing result is used as the time-varying estimate of the rest wavelength, from which the Doppler shifts, and hence line-of-sight velocities, are calculated. The uncertainties associated with line-of-sight wind estimates vary, depending primarily on the emission brightness. We have not attempted to present spatially and temporally varying estimates of the uncertainties associated with the wind measurements described here. Rather, we simply note that the uncertainties associated with individual line-of-sight wind estimates seldom exceed 20 to 25 $\mathrm{m\,s^{-1}}$.

3.2. Wind Vector Estimation

The Doppler technique only measures the line-of-sight component of what is, in reality, a three-component vector wind field. It is not possible to infer unambiguously all three components of the actual wind (northward, eastward, and upward) solely from a single station's line-of-sight data. However, by applying certain assumptions, it is possible to uniquely determine the vector field that would generate the observed line-of-sight velocities if those assumptions held. Although this is not entirely satisfactory, visual interpretation of wind vectors is considerably easier than it is for line-of-sight data.

We resolve the total wind field into two contributions: a scalar vertical wind and a two-component vector horizontal wind. Our first assumption is that the vertical wind is constant across the entire region of sky viewed by the instrument. This assumption is known to be incorrect in the auroral zone. Spatial structure has been observed in the horizontal distribution of thermospheric vertical wind in the auroral zone [e.g., *Price et al.*, 1995; *Innis et al.*, 1996]. However, thermospheric vertical winds are normally small compared to the typical horizontal winds of hundreds of $\mathrm{m\,s^{-1}}$, except during isolated "events" [*Conde and Dyson*, 1995b]. Further, the viewing geometry is such that the line-of-sight component of the vertical wind decreases with increasing horizontal distance from the instrument's zenith point. These two effects, in combination, suggest that serious

distortions of the inferred horizontal wind field due to spatial nonuniformity of the vertical wind occur only infrequently and should not alter the conclusions presented here.

Our estimation of the horizontal vector wind field is based on the method described by *Browning and Wexler* [1968] for analyzing tropospheric Doppler radar data. This method was applied to thermospheric airglow spectra by *Burnside et al.* [1981] and extended to allow estimation of total vorticity. However, unlike these authors, we only used the method to infer the component of the horizontal wind normal to our instrument's line of sight. In all the plots presented here, the horizontal wind components parallel to the instrument's line of sight are directly as measured.

Consider an instrument sampling spectra from a set of annular regions in sky. Each annulus is centered about the zenith, with a "radius" which is specified as a zenith angle ϕ. Further, let each annulus be divided in azimuth into n equal-sized sectors, with the kth sector being centered on an azimuth angle of θ_k. For a given annulus at zenith angle ϕ, we will use the set of line-of-sight wind measurements at each azimuthal angle θ_k to derive estimates of the wind vectors. We denote this set as $\{V^{\parallel}(\theta_k, \phi)\}$.

A uniform vertical wind V_z would produce a velocity component parallel to the instrument's line of sight given by

$$V^{\parallel}(\theta_k, \phi) = V_z \cos\phi. \tag{1}$$

We define a positive V_z to be an upward wind, in accordance with convention. Notice that the line of sight component of a uniform vertical wind is constant for all azimuth sectors. A uniformly divergent horizontal wind receding at the same speed in all azimuth sectors at a speed ε would also produce a constant line-of-sight component in all azimuth sectors, given by

$$V^{\parallel}(\theta_k, \phi) = \varepsilon \sin\phi. \tag{2}$$

Thus within a single annular sampling region the instrument cannot distinguish between uniform vertical flow and uniform horizontal divergence. Notice, however, that the zenith angle dependency of these two contributions is different, allowing them to be resolved by considering several annuli spanning a range of values of ϕ. For the single small observing spot centered in the zenith, we have $\phi = 0$ and $n = 1$. Equations (1) and (2) indicate that in this case the only contribution to $V^{\parallel}(\theta_k, 0)$ is due to the vertical wind and that

$$V_z = V^{\parallel}(\theta_1, 0), \tag{3}$$

with θ_1 being retained solely for consistency of notation; its value has no effect in this expression. Since we are assuming the vertical wind is uniform throughout the instrument's field of view, we can use this result to remove the vertical wind contribution to the line-of-sight wind in each of the observed zones. This yields a new, corrected, set of line-of-sight winds which should contain only contributions due to the horizontal wind field; we denote it as $\{H^{\parallel}(\theta_k, \phi)\}$. The kth element of $\{H^{\parallel}\}$ at zenith angle ϕ is related to the corresponding element in $\{V^{\parallel}(\theta_k, \phi)\}$ by

$$H^{\parallel}(\theta_k, \phi) = V^{\parallel}(\theta_k, \phi) - V_z \cos\phi. \tag{4}$$

The horizontal wind velocity component parallel to the instrument's line-of-sight seen when viewing in the kth azimuthal sector is related to the total horizontal wind vector by

$$H^{\parallel}(\theta_k, \phi) = \sin\phi(H_x \sin\theta_k + H_y \cos\theta_k) \tag{5}$$

where, consistent with our upward vertical wind convention, a positive value of $H^{\parallel}$ indicates a receding wind, and H_x and H_y denote the spatially varying zonal and meridional wind fields, respectively.

We approximate the total horizontal vector wind field using first-order Taylor series expansions of the zonal and meridional components about the zenith,

$$H_x = u_0 + \frac{\partial u}{\partial x}x + \frac{\partial u}{\partial y}y \tag{6}$$

$$H_y = v_0 + \frac{\partial v}{\partial x}x + \frac{\partial v}{\partial y}y, \tag{7}$$

where x and y are the zonal and meridional distances from the zenith to an observation point at zenith angle ϕ and azimuth angle θ. That is,

$$x = R\sin\theta \tag{8}$$

$$y = R\cos\theta \tag{9}$$

$$R = h\tan\phi, \tag{10}$$

with h being the height of the emission layer.

The actual observed line-of-sight wind component may be represented as a Fourier series by

$$H^{\parallel}(\theta_k, \phi) = \{a_0 + \sum_{m=1}^{\frac{n}{2}-1}(a_m \sin m\theta_k + b_m \cos m\theta_k)\}\sin\phi. \tag{11}$$

This may be inverted to give the Fourier coefficients,

$$a_0(\phi) = \frac{1}{2n\sin\phi}\sum_{k=0}^{n-1} H^{\parallel}(\theta_k, \phi), \tag{12}$$

$$a_m(\phi) = \frac{1}{n\sin\phi}\sum_{k=0}^{n-1} H^{\parallel}(\theta_k, \phi)\sin m\theta_k, \tag{13}$$

$$b_m(\phi) = \frac{1}{n\sin\phi}\sum_{k=0}^{n-1} H^{\parallel}(\theta_k, \phi)\cos m\theta_k, \tag{14}$$

with (13) and (14) being evaluated for $m = 1$ to $m = n/2 - 1$.

Browning and Wexler [1968] and *Burnside et al.* [1981] used (5)-(11) to derive expressions relating the Fourier coefficients a_m and b_m to the unknown terms in the Taylor series expansions (6) and (7) above. They

(and others [e.g., *Batten et al.* 1988]) show that the $m = 1$ coefficients correspond to the uniform wind terms in the Taylor series above, with $u_0 = a_1$ and $v_0 = b_1$.

The partial derivatives in (6) and (7) are related to the $m = 0$ and $m = 2$ coefficients. However, since there is only one nonzero $m = 0$ coefficient, there are only three Fourier coefficients from which to compute four partial derivatives. Thus the line-of-sight wind data from a single "exposure" of the instrument is not sufficient to uniquely define all the terms in the two Taylor series. The practical result of this is that it is impossible to estimate simultaneously both the total divergence ($\partial u/\partial x + \partial v/\partial y$) and the total vorticity ($\partial v/\partial x - \partial u/\partial y$) from a single exposure.

The *Burnside et al.* [1981] method extends that of *Browning and Wexler* [1968] by using information from several consecutive exposures. The final constraint needed for a unique solution is obtained by assuming that at least over short time intervals

$$\frac{\partial v}{\partial x} \simeq \frac{1}{\epsilon}\frac{\partial v}{\partial t}, \tag{15}$$

where ϵ is the tangential velocity of the observatory due to the rotation of the Earth. The assumption is that for sufficiently short time intervals the rotation of the Earth can be regarded as moving the station through a meridional wind field that is stationary in local time. This allows the meridional wind to be sampled at various locations along the zonal direction, which is not possible using line-of-sight data from a single observation. There are times when this approximation will be invalid in the auroral zone. This would be the case whenever the wind field seen in latitude/local time coordinates was not stationary. For example, the interplanetary magnetic field's "Y" component is known to influence the thermospheric circulation at high latitudes [e.g., *McCormac and Smith*, 1984; *Sica et al.*, 1989; *McCormac et al.*, 1991]. During a sudden change in IMF B_y, (15) would presumably be a poor approximation.

In this experiment, $\partial v/\partial t$ at the jth time interval t_j was estimated from our set of estimates of the uniform component of the meridional wind as a function of time $\{v_0(t_j)\}$. That is, we used the central difference approximation,

$$\frac{\partial v(t_j)}{\partial t} \simeq \frac{v_0(t_{j+1}) - v_0(t_{j-1})}{t_{j+1} - t_{j-1}}. \tag{16}$$

In practice, the set $\{v_0(t_j)\}$ was three-point smoothed prior to evaluating (16), in part to suppress the noise enhancements associated with numerical differentiation. Thus our method for obtaining $\partial v/\partial t$ (and hence $\partial v/\partial x$) was based on instrument exposures taken approximately 45 min apart. The time constant for the thermosphere to respond to a change in ion drag forcing is typically an hour or more [e.g., *Killeen et al.*, 1984; *Meriwether et al.*, 1988], although it can drop below 50 minutes in regions of enhanced electron density such as the cusp and the evening auroral zone [*Smith et al.*, 1988]. Our own data, presented here, does contain examples of changes on timescales as short as 30 min or less. Unfortunately, it is difficult to tell whether these arise because of temporal changes to the large-scale flow, or because the observatory is moving under a "front" in a flow pattern which is stationary in local time. In the case of rapid temporal evolution, our application of the *Burnside et al.* [1981] method of estimating $\partial v/\partial x$ must introduce some distortions, although the three-point smoothing of $\{v_0(t_j)\}$ will act to suppress these errors. Also, any such errors only effect two of the four partial derivatives ($\partial v/\partial x$ and $\partial u/\partial y$) used to estimate the spatial variation of one component (the perpendicular component) of the total wind field. In most cases, the time constant for changes in meridional wind does appear long enough for the method not to introduce significant distortions in the perpendicular component.

Overall, we expect neither the assumption contained in (15), nor our application of this assumption through (16), to alter our fundamental conclusions. Indeed, the results we present here support this statement to some extent. Our estimate of $\partial v/\partial x$ is obtained directly from $\partial v/\partial t$, using (15). Thus, if temporal changes in the wind field were significant (after scaling to an equivalent spatial gradient using the Earth's rotation velocity) then we would expect our results to contain examples of large (but spurious) $\partial v/\partial x$ values. Although our inferred vector wind fields frequently show spatial variations, there are actually very few cases showing a large change of meridional wind with longitude. That is, $\partial v/\partial x$ usually appears small compared to both the mean wind and to the other three partial derivatives, $\partial v/\partial y$, $\partial u/\partial y$, and $\partial u/\partial x$. This is not unreasonable; latitudinal gradients generally exceed longitudinal ones in the auroral zone. The only way that a large temporal change could fail to be interpreted as a large $\partial v/\partial x$ variation is if the actual $\partial v/\partial x$ spatial variation at the time almost exactly cancelled the temporal change. Such cancellation would need to happen most of the time to be consistent with our data set. We consider this unlikely.

Having estimated the zonal and meridional wind components using the Taylor series expansions, it is straightforward to compute the component of this fitted wind field that lies perpendicular to the instrument's line of sight. That is,

$$H^{\perp}(\theta_k, \phi) = H_x \sin\theta_k - H_y \cos\theta_k. \tag{17}$$

Finally, we compute our "best estimate" of the meridional and zonal components of the actual horizontal wind field by combining the observed line-of-sight components with the fitted components normal to the line of sight. We can do this in all fields except the central, zenith, one. That is,

$$H_x(\theta_k, \phi) = \frac{H^{\parallel}(\theta_k, \phi)}{\sin\phi}\cos\theta_k + H^{\perp}(\theta_k, \phi)\sin\theta_k. \tag{18}$$

$$H_y(\theta_k, \phi) = \frac{H^{\parallel}(\theta_k, \phi)}{\sin\phi}\sin\theta_k - H^{\perp}(\theta_k, \phi)\cos\theta_k. \tag{19}$$

Once again, it is stressed that this vector field contains

all of the features of the original thermospheric horizontal wind in the line-of-sight direction but possibly distorts or fails to include part of the structure that was originally present in the perpendicular direction.

Note that the above analysis has regarded each annular set of observing zones independently, so the method could actually be applied to compute different values for the partial derivatives in (6) and (7) for each annulus. There are two problems with this. First, the annulus immediately surrounding the zenith spot was only allocated four sectors, which is not sufficient to fit the six coefficients needed to evaluate the Taylor series. Second, because the partial derivatives are calculated effectively by looking at differences across the sky, it seems inappropriate to allow different values to apply for the inner annuli than for the surrounding outer annuli. Thus for the results presented here the partial derivatives were calculated independently for the outer two annuli of observing zones, but averages of these two sets of results were used over the whole sky when evaluating the Taylor series. The $m = 1$ uniform wind terms were calculated and applied independently in all annuli, however.

Figure 1 presents six examples of horizontal wind vector fields inferred using the above described method, superimposed directly onto the line-of-sight measurements from which they were derived. In compiling this figure we have selected a variety of inferred vector wind

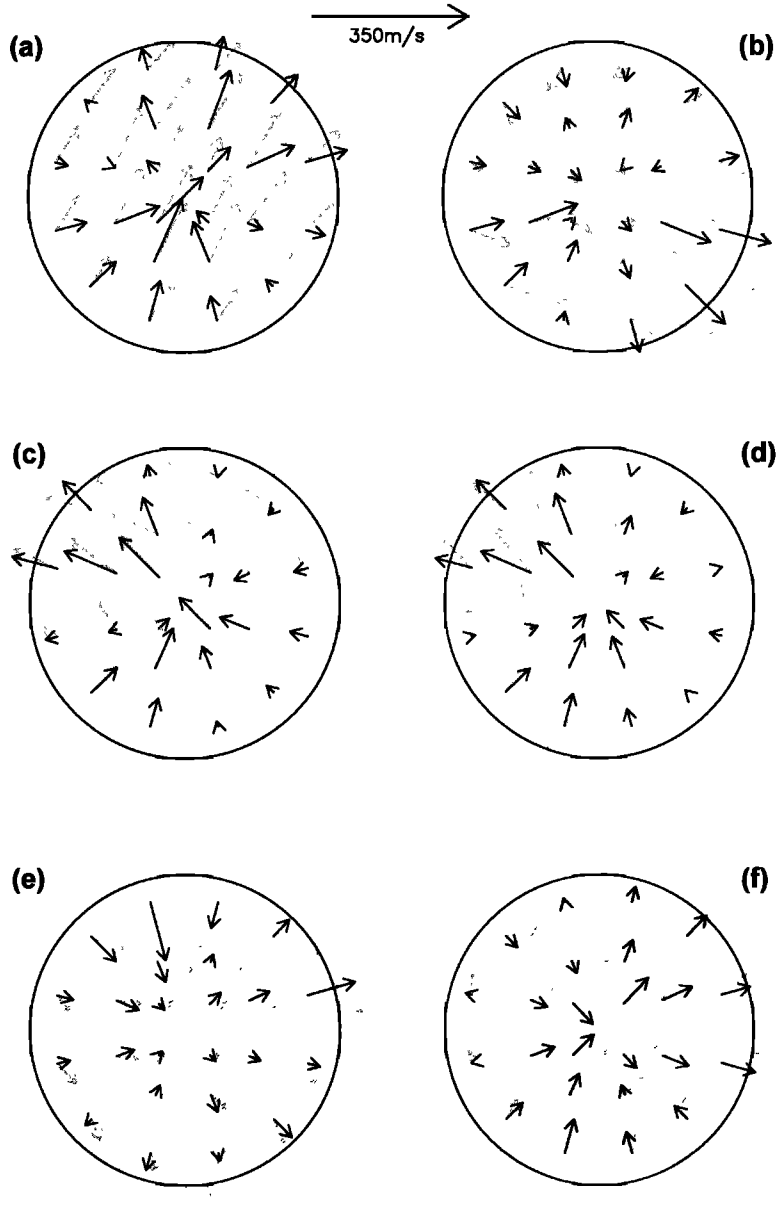

Figure 1. Six examples showing observed line-of-sight winds (black arrows) and the vector fields that our analysis infers from them (grey arrows). North is at the top and east is to the right. The six times shown are (a) 0246 UT on November 15, 1996, (b) 0701 UT on November 8, 1996, (c) 0716 UT on November 15, 1996, (d) 0901 UT on November 17, 1996, (e) 1231 UT on November 17, 1996, and (f) 1100 UT on January 11, 1997.

patterns, to allow readers to make their own assessment of our experiment's performance over a range of actual conditions. The six vector flow configurations presented are uniform northeastward flow (Figure 1a), eastward flow in the south shearing to doldrums in the north (Figure 1b), northeastward flow in the south shearing with latitude to become westward flow in the north (Figures 1c and 1d), east or southeastward flow in the north and northeast shearing to doldrums in the south and southwest (Figure 1e), and northward flow in the south converging with eastward flow over most of the rest of the sky (Figure 1f).

Clearly, these vector fields are not uniquely determined by the observations themselves; the fitted vectors are only unique within the assumptions contained in the analysis method. To assess the method, the reader must decide whether reasonable departures from its assumptions would significantly modify the inferred vectors and, further, whether this would be likely to occur often. In our experience the method rarely produces implausible vector fields, and, further, its results are almost always consistent with geophysical conditions and with data from other instruments. (Detailed comparison with data from other instruments will be pursued in a subsequent paper.) Since both our instrument and our implementation of the *Burnside et al.* [1981] method are new, we do suggest that the results presented here be regarded as preliminary and, as yet, unvalidated. Such validation would require simultaneous observations using both our technique and some other method, independently capable of resolving spatial structure in the thermospheric wind field. For example, several rockets could be launched along slightly divergent trajectories and used to release chemical wind tracers nearly simultaneously at multiple spatial locations. This would allow a very direct measurement of the spatial variation of the wind, but only for a brief time interval. If good agreement were found with the imaging FPS data, we could then use the FPS more confidently for long-term monitoring.

4. Observations

4.1. Data Selection

The instrument was operated from mid October through early May of the 1996/1997 northern winter. Observations were conducted on nights when the Moon's near side was less than about 50% illuminated. Under a full or near-full Moon, the signal-to-noise ratio of the recorded spectra became unacceptably low. We believe this was partly due to moonlight scattering in the all-sky optics, and partly due to geometric distortion of the IPD image when there was a dominant, very bright spot in the field of view. The sky conditions (i.e., extent and nature of cloud cover) were assessed for each observing night using a combination of data from an all-sky camera and from a four-channel meridian scanning photometer, both colocated at Poker Flat with the ASI-FPS. Data from cloudy periods were rejected. (Although it is often possible to identify cloudy periods from the wind data itself, we used the other instruments to ensure independent verification of the clarity of seeing.)

Many interesting phenomena appear in these data. Here we present a few selected examples of inferred flow structures with horizontal scale sizes smaller than our field of view (of diameter ~1000 km). We chose these particular days by first visually examining the analysis results from all observing periods, to gain an overall impression of the behavior of the wind systems during the winter. We then selected 6 days which included clear examples of the phenomena that appeared important to understanding the range and the variability of these wind systems across the whole data set.

In practice, there was considerable day-to-day variability in the observed winds. For our location, and for the solar minimum period examined here, it appeared that most of this day-to-day variability was associated with degree to which ion drag forcing was able to establish sunward flow in the afternoon and evening sectors. There was also a strong seasonal effect, with sunward flow in the evening being much less probable in December, January, and February than it was before midwinter or in late spring. These findings are similar to those reported by *Conde and Dyson* [1995a] based on southern auroral-latitude observations from Mawson, Antarctica. The day-to-day variability that we observed is the reason that we have chosen to present "representative" days, rather than attempt to examine average patterns based on some strategy for binning subsets of the whole data. Our main objective in this study was to examine small-scale nonuniformity of the thermospheric wind. Even though several persistent small-scale features were identified in the data, it seemed likely that their appearance would be distorted or suppressed by averaging over multiple days.

4.2. Geophysical Conditions

The geophysical conditions prevailing on each of the nights presented here are summarized in Tables 1 to 3. We include these brief descriptions of IMF conditions merely as a convenience. Proper time series plots of the IMF values for each of these periods are available from the "cdaweb" world-wide-web service, at the URL http://cdaweb.gsfc.nasa.gov/ cdaweb/istp_public/.

4.3. October 17, 1996

On magnetically quiet days around midwinter, the observed wind fields remained relatively uniform, blow-

Table 1. Solar and Magnetic Activity

Date	A_p	$F_{10.7}$
Oct. 17, 1996	6	69
Nov. 08, 1996	4	69
Nov. 15, 1996	11	74
Nov. 17, 1996	12	72
Jan. 11, 1997	13	74
March 6, 1997	8	75

Table 2. IMF B_z Conditions

Date	IMF B_z
Oct. 17, 1996	A few nanoteslas positive before 08 UT, a few nanoteslas negative after 08 UT
Nov. 08, 1996	A few nanoteslas negative before 11 UT, a few nanoteslas positive after 11 UT
Nov. 15, 1996	Variable within ±6 nanoteslas
Nov. 17, 1996	Variable within ±5 nanoteslas
Jan. 11, 1997	+20 nanoteslas at 05 UT, decaying to near 0 by 08 UT
March 6, 1997	A few nanoteslas positive before 13 UT, a few nanoteslas negative after 13 UT

ing roughly magnetically northeastward early in the night, and turning toward the southeast as the night progressed. For example, Figure 2 shows an overview of the evolution of the thermospheric wind field during the night of October 17, 1996. The "clock dial" layout of this plot is similar to that often used to display thermospheric winds recorded at high-latitude sites, except that in this case we show complete sky maps of the wind field as a function of time, rather than the traditional one or two vectors for each time. The figure is intended to show the evolution of the wind field above Poker Flat as seen by an observer located in space, some distance above the north geomagnetic pole. The direction to the Sun is toward the top of this figure so, as time advanced, the spaced-based observer would see the observatory move anticlockwise in a circular arc centered on the magnetic pole. Each successive set of vectors in a circle maps the wind field measurable from Poker Flat, at ~75 min intervals, and is labeled with the corresponding universal time. (Although we usually observed using 15 min exposures, Figure 2 can only show every fifth exposure without overlap because the diameter of the field-of-view circles has been scaled correctly relative to the distance to the magnetic pole.) The arrows have been positioned within each circle so that their centers indicate the relative geographic locations of the observing zones. This is different from the more usual convention of positioning the arrows so that their tails represent the measurement location. After comparing both presentations we chose to use center-based locations because the eye seemed to assign positions based on arrow centers rather than ends. (Note that we did use the tail-based location convention for Figure 1 to facilitate comparison of two sets of arrows.)

Of 79 nights examined, roughly 40% behaved similarly to the night shown in Figure 2. We interpret this relatively uniform and generally eastward wind as being driven in the premidnight sector principally by the global-scale pressure gradient associated with solar heating and by a combination of pressure gradient and ion drag postmidnight. The pattern of flow depicted in Figure 2 is very similar to those reported for geomagnetically quiet conditions by *Niciejewski et al.* [1996], who observed with a Fabry-Perot spectrometer located at Watson Lake in the Yukon Territory. Their instrument recorded Doppler shifts of λ630 nm emissions between November 1991 and April 1993. Although Watson Lake is geographically further south than Poker Flat (by ~5°), its magnetic latitude is the same. The two sites are only ~1000 km apart, so similar winds would be expected at each. The Watson Lake data were taken at a time closer to solar maximum than our observations presented here. Even so, the large-scale wind patterns seen in the two data sets are, indeed, similar.

4.4. November 15, 1996

Figure 3 shows an overview of the evolution of the thermospheric wind field during the night of November 15, 1996, in the same format as figure 2. Westward (i.e. sunward) flow is apparent poleward of the observatory between 0616 and 0846 UT. Even earlier, at 0501 UT, the wind poleward of the observatory had not yet turned sunward, but it was noticeably weaker than the strong antisunward flow equatorward of the observatory.

To present the data at its full time resolution of around 15 min, we need to abandon the clock dial layout of Figures 2 and 3. Instead, we simply plot all the wind vector maps in a rectangular array, as shown for the November 15 data in Figure 4. Note that the directions used to plot each of the wind maps are rotated with time such that these plots could be rearranged to form a dial plot, similar to Figures 2 and 3. Each plot in Figure 4 includes an "index" arrow, which points geomagnetically poleward. The index arrow also indicates whereabouts that plot falls on a dial format layout. For example, the arrow on the map for 0501 UT points horizontally, toward the right. If this map were placed at

Table 3: IMF B_y Conditions

Date	IMF B_y
Oct. 17, 1996	Variable – mostly a few nanoteslas negative before 07 UT, a few nanoteslas positive after 07 UT
Nov. 08, 1996	A few nanoteslas positive before 12 UT, a few nanoteslas negative after 12 UT
Nov. 15, 1996	A few nanoteslas positive before 08 UT, up to 20 nanoteslas positive after 08 UT
Nov. 17, 1996	Generally a few nanoteslas positive, except for about 5 nanoteslas negative 11-13 UT
Jan. 11, 1997	Variable before 08 UT, a few nanoteslas positive after 08 UT
March 6, 1997	Highly variable within ±5 nanoteslas

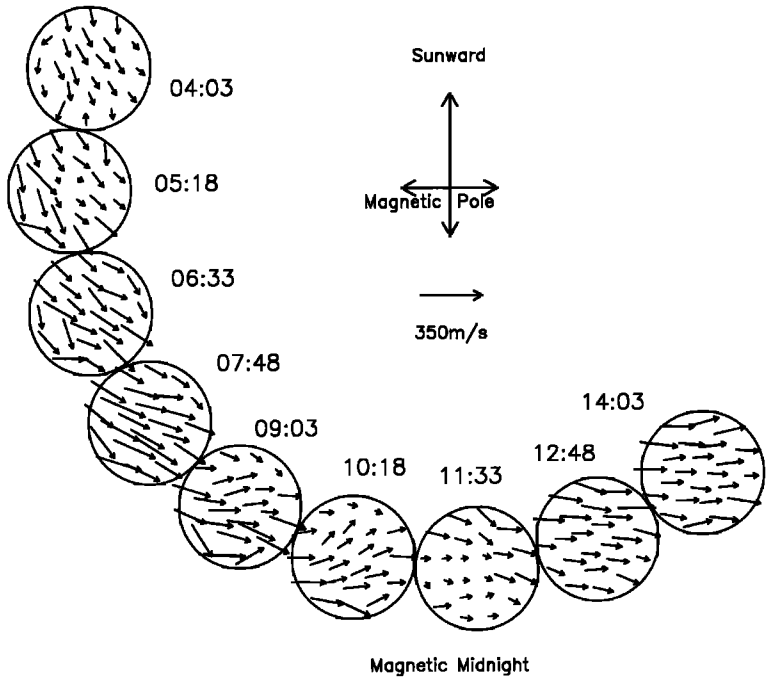

Figure 2. Evolution of the thermospheric horizontal vector wind field on the night of October 17, 1996. See text for an explanation of the format of this plot. Times indicated are in UT.

the "9 o'clock" position on a clock dial then the index arrow would point poleward. Comparison with Figure 3 shows that, indeed, at the "9 o'clock" position, we do find the wind vector map for a universal time of 0501, and that its orientation matches that of the 0501 map in Figure 4. As another example, the arrow on the 1231 vector map in Figure 4 indicates it should correspond to the map appearing at approximately the "5 o'clock"

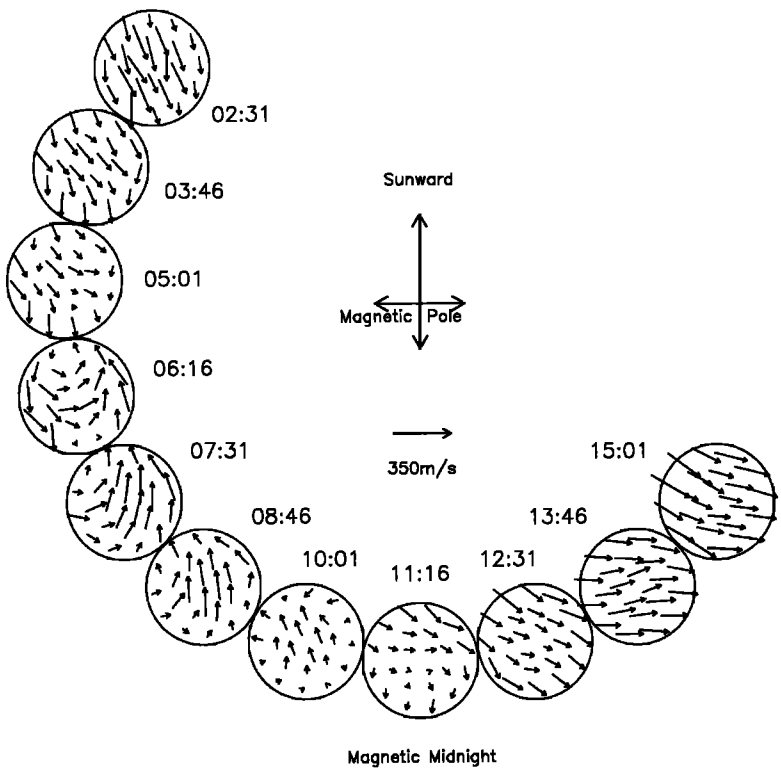

Figure 3. Evolution of the thermospheric horizontal vector wind field on the night of November 15, 1996.

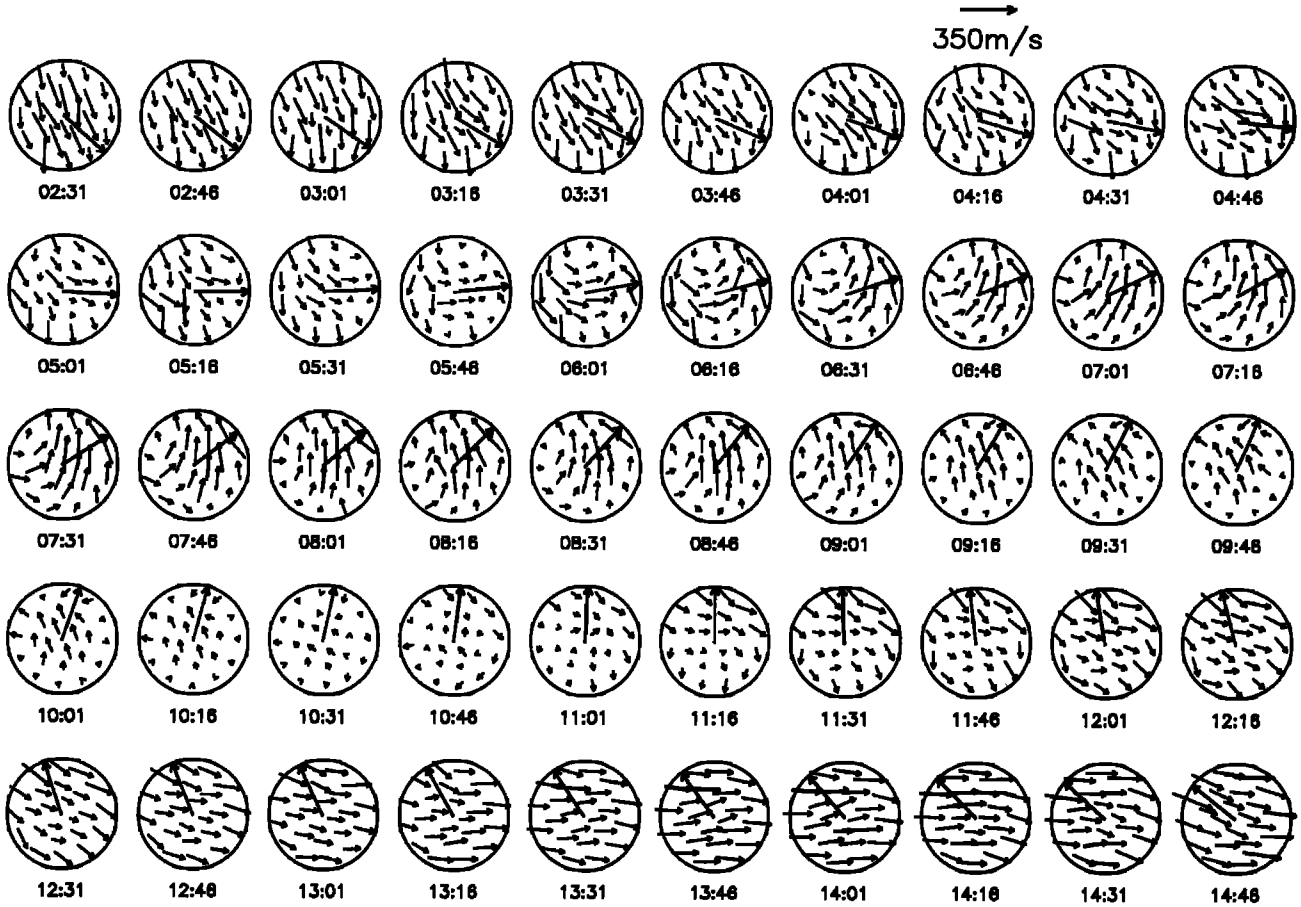

Figure 4. Evolution of the thermospheric horizontal vector wind field on the night of November 15, 1996. This figure shows the same data as figure 3 but at the full time resolution of 15 min. Here the wind maps have been reorganized from the previous "dial" format into a simple rectangular array. The radial arrow in each circle points magnetically poleward and indicates whereabouts that circle would fall around the "dial" in a diagram of the format of Figures 2 and 3.

location on Figure 3. Again, this is so. As in Figures 2 and 3, the sunward direction is toward the top of the page in all cases.

November 15, 1996, is representative of an overall wind pattern that appeared very commonly in our data, that is, on at least one third of all nights (and in an even higher proportion outside of the months of December, January and February). Prior to about 1000 UT, the aurora lay well north of the observatory and was quite active at times. A breakup began just before 1000 UT, so that there was active aurora overhead until about 1400 UT, when the arcs reformed in the north and remained there for the rest of the night. The wind blew uniformly antisunward early in the night, as expected for winds driven mainly by the pressure gradient established by solar heating. As the evening advanced, Poker Flat began to move under the expected region of eveningside sunward ion convection. The effect (presumably) of this was seen in the neutral wind, which also turned basically sunward by ~0800 UT. Notice that throughout the period from around 0530 UT until just before magnetic midnight, the wind flow was not uniform. We interpret this as indicating that Poker Flat was passing under a transition region, such that the neutral flow equatorward of the observatory was responding mostly to pressure gradient forcing, whereas poleward of it ion drag forcing dominated the observed flow.

Just prior to magnetic midnight there was a "doldrums" period (at ~1031 UT). This may merely indicate that the large-scale spatial variation of external driving forces and of inertial "forces" acting on the wind was such that they drove the wind to zero around this time. (Note that this is not the same as having the forces sum to zero, which would mean that there was no acceleration and that a preexisting wind would continue blowing unabated.) Interestingly, the time of wind doldrums also corresponded to the most active period of the auroral breakup. We plan future studies to test whether this was more than coincidental.

In the 90 min or so around magnetic midnight (~1120 UT) we see an example of another commonly observed spatial structure in the wind above Poker Flat. This is the presence of a sharp front in the flow, corresponding to the eveningside edge of the so-called "cross-polar jet." Beginning with the 1046 UT exposure, the cross-polar jet was observed as magnetic southeastward flow appearing at the north and northeast edge of the in-

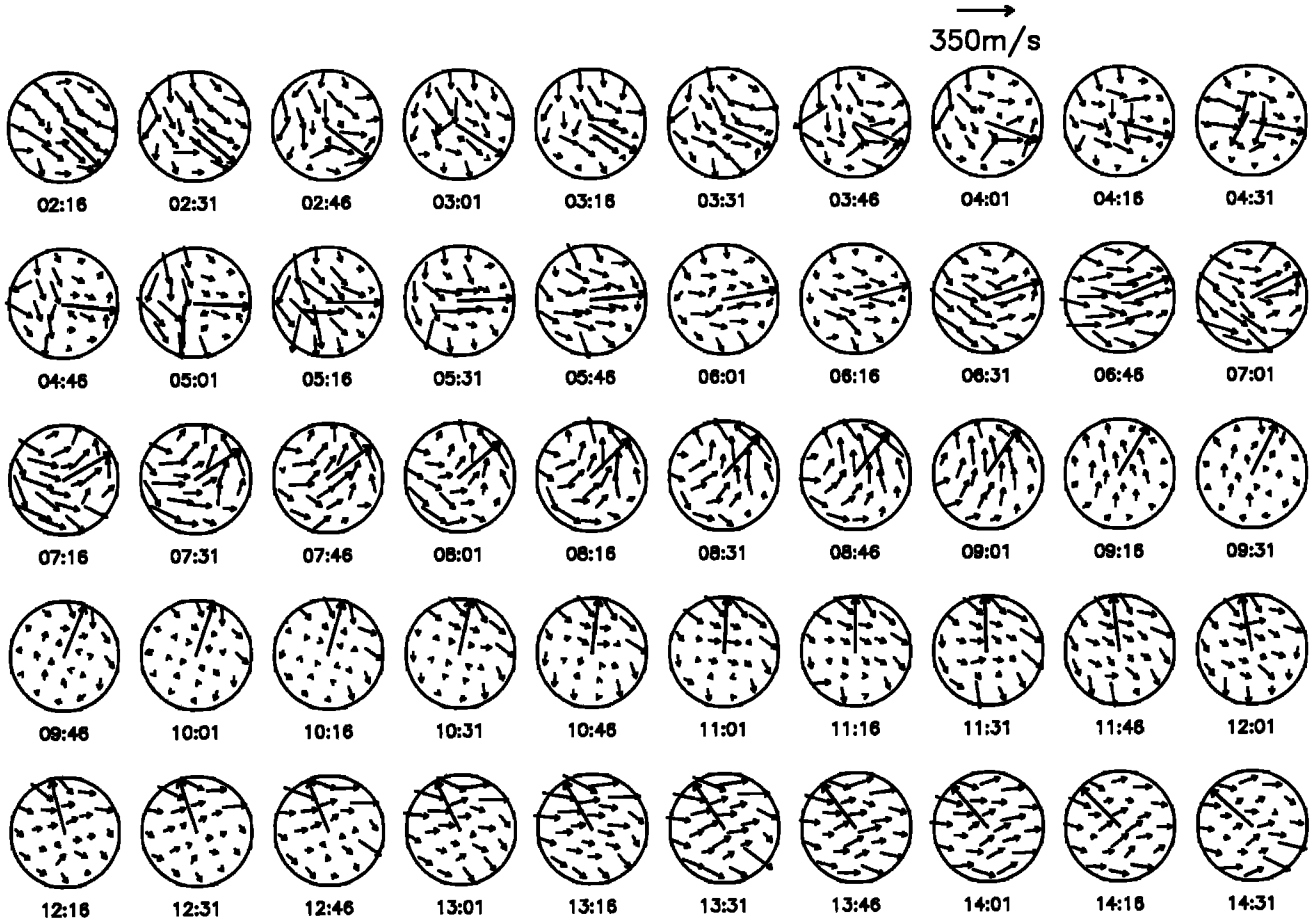

Figure 5. Evolution of the thermospheric horizontal vector wind field on the night of November 17, 1996.

strument's field of view. During the following 90 min this feature advanced across the field of view so that by 1216 UT the entire sky lay within the jet, and the flow was relatively uniformly directed southeastward in all viewing directions. After that time the flow remained relatively uniform for the rest of the night and was dominated by the cross-polar jet emerging from the polar cap.

4.5. November 17, 1996

This night was similar to November 15 and is shown in Figure 5. All-sky camera observations of the aurora did not commence until around 0700 UT, at which time bright, active arcs lay north of the observatory. A breakup began at around 0900 and was followed by pulsating aurora until around 1031 UT. After that a single arc reformed just north of the observatory and remained there for the rest of the night. At the start of Fabry-Perot observations the wind was blowing geomagnetically poleward and antisunward, as it was 2 days earlier. However, from about 0246 UT onward we see the signature of ion drag acting poleward of the observatory and attempting to turn the wind westward (which would also be sunward in this dusk time sector). This behavior appeared 2 to 3 hours earlier than on November 15. Although the ion drag signature manifested itself earlier on November 17, it was not powerful enough to sustain the westward winds until about 0701 UT. Thus between 0246 and 0701 UT on November 17 the wind field exhibited varying levels of shear with latitude. Between around 0716 UT and 0916 UT the flow became highly sheared, highly curved, and contained a well-developed westward/sunward flow poleward of the observatory.

A brief period of doldrums occurred when the westward/sunward flow collapsed at around 0931 UT, roughly an hour earlier than the corresponding event on November 15. The onset of the doldrums again followed an auroral breakup, which began around 0900 UT. The edge of the cross-polar jet was sighted poleward of the observatory as early as 0946 UT. This was almost immediately after the collapse of the sunward flow. By contrast, the edge of the jet was not seen on November 15 until 1046 UT. On November 17 the edge of the jet advanced equatorward until ~1201 UT but then retreated poleward for an hour or so. Finally, by around 1316 UT the jet covered the whole sky, and relatively uniform east-southeastward flow prevailed from then on, albeit not as strongly as 2 days previously.

4.6. November 8, 1996

The aurora was less active on this night than on the 2 nights described above, particularly early in the evening. As depicted in Figure 6, westward flow pole-

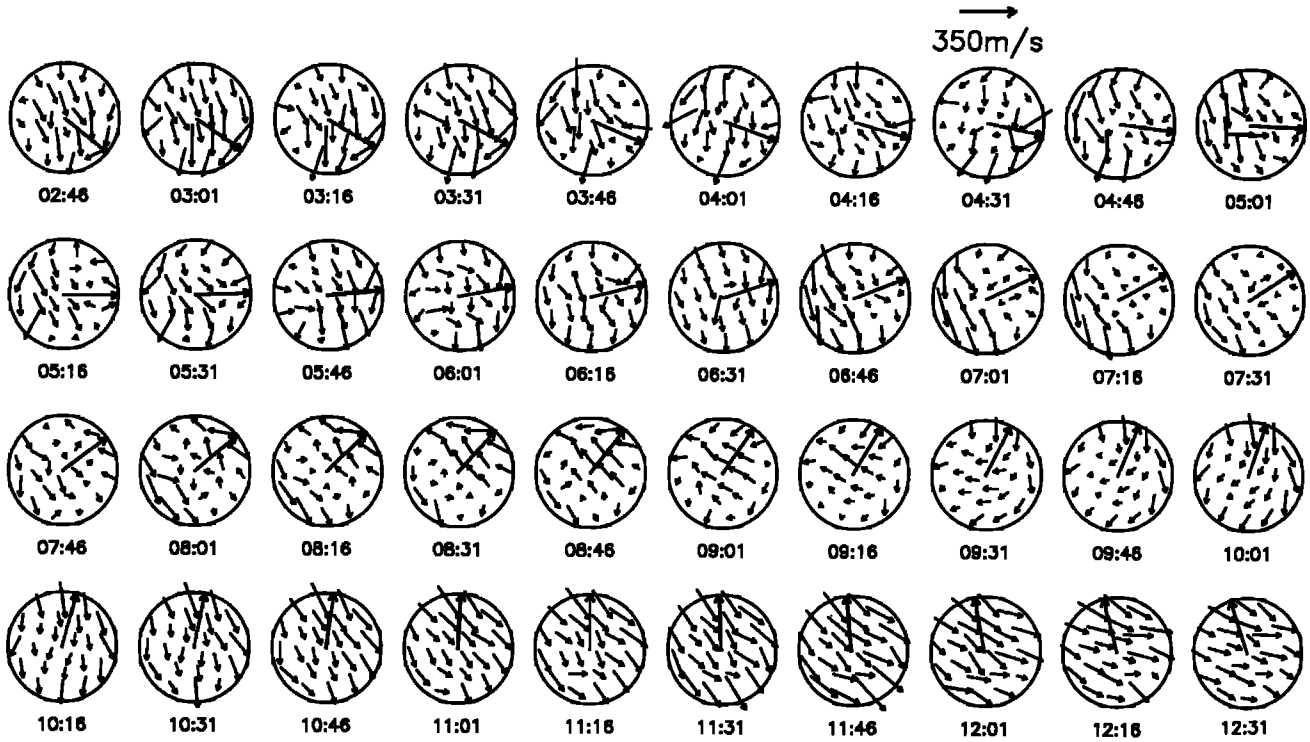

Figure 6. Evolution of the thermospheric horizontal vector wind field on the night of November 8, 1996.

ward of the observatory did not really develop until around 0746 UT. The data between about 0446 and 0516 UT exhibited weakened antisunward flow poleward of the observatory, indicating some attempt to drive the wind westward/sunward. A similar gradient appeared after about 0646 UT, and eventually evolved into the flow seen at 0746 UT and following. Although we believe that the flow poleward of the observatory between 0746 and about 0846 UT was almost certainly driven by ion-drag, it was different in character to the flow at this time in the two examples above. On both of those nights, the shear from eastward to westward flow with increasing latitude occurred mainly as a rotation of the vectors, so that winds blew poleward at the latitude of the observatory. The resulting flow patterns looked like partial vortices. In particular, air parcel trajectories would carry them from the low-latitude antisunward flow into the higher-latitude sunward flow. On November 8 the shear with latitude was present, but there was no connecting flow across the shear, at least within the region visible from the observatory. Thus, unless this connecting flow lay outside our field of view, we presume that low-latitude air parcels were not being fed into the sunward flow, as they were in the previous examples.

Some time around 0846 UT the flow poleward of the observatory encountered the edge of the cross-polar jet. The result was a gradual anticlockwise rotation of the flow poleward of the observatory, accompanied by a steady advance of the cross-polar jet across our field of view. During this transition the flow became noticeably curved so that air parcel trajectories would have been deflected to the right, as seen by an observer looking in the direction of travel of a parcel. By 1046 UT the cross-polar jet covered the entire visible sky, and relatively uniform wind prevailed, again directed southeastward. No period of doldrums was observed on this night.

4.7. March 6, 1997

This day was characterized by bright, active, aurora poleward of the observatory early in the evening, which then moved equatorward so that after about 0830 UT the aurora was overhead or south of the observatory and remained so for the rest of the night. Due to the season, the observations shown in Figure 7 could not commence until 0516 UT. The zonal wind was blowing eastward (antisunward), but the meridional wind was more strongly poleward than typically seen in our data at this time. Over the next 3 hours the wind turned sunward, but in this case the transition occurred as a smooth anticlockwise rotation of a relatively uniform wind field. It was not accompanied by the curvature and shear that usually appeared on days with a transition to sunward wind in the evening (such as November 15 and 17, 1996, discussed above). The reason for this is unknown, although it may simply indicate that the shear extended over a spatial region several times larger than our field of view, so that the portion of it visible to our instrument appeared uniform.

At 0846 UT, the evening-side edge of the cross-polar jet reached the furthest poleward zones in our field of

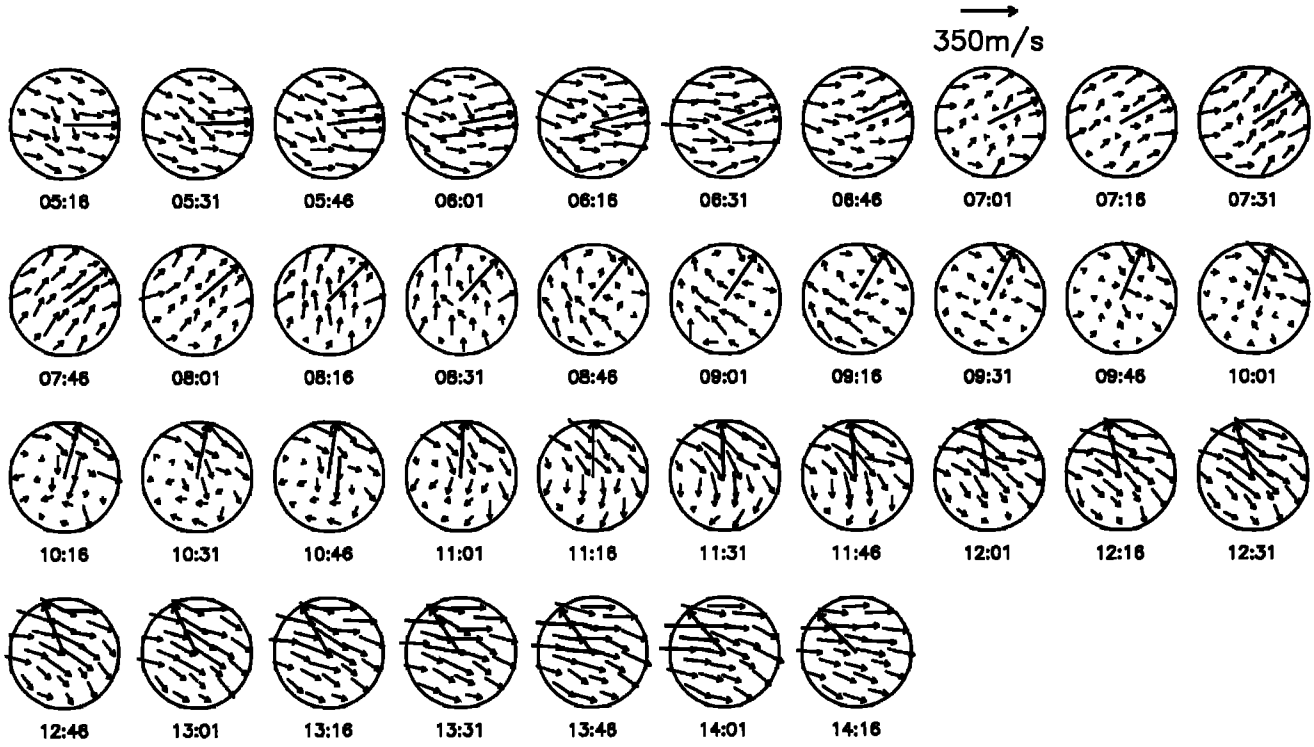

Figure 7. Evolution of the thermospheric horizontal vector wind field on the night of March 6, 1997.

view. Over the next 3 hours considerable shear and curvature of the flow occurred within our field of view. Between 0901 and 1046 UT the cross-polar jet flowed eastward or southeastward in regions poleward of the observatory, whereas equatorward of the observatory ion drag drove the wind westward (although the strength of this westward flow varied). For the remainder of the night, the cross-polar jet changed only gradually poleward of the observatory, by advancing across our field of view, and rotating slowly toward the south. The southward rotation was such that, seen in the Sun-aligned coordinates of Figure 7, the wind direction actually appeared relatively constant. However, equatorward of the observatory, the wind turned strongly anticlockwise, so that westward flow at 1031 UT had become southeastward flow by 1231 UT. The net effect of these changes between 0901 and 1231 UT was to gradually reduce the amount of wind shear above our observatory. The flow after 1231 UT was slightly divergent and slightly curved, but not noticeably sheared.

The appearance of the cross-polar jet at 0846 was an hour earlier than when it was seen even on November 17, 1996. This is consistent with the observation that the aurora moved equatorward of the observatory just before this time. These two observations suggest that both the auroral oval and the ion convection pattern had expanded to lower latitudes than usual. On this night the observatory appeared to pass under the poleward edge of the region of late evening sunward flow, so that at around 0916 UT, for example, westward flow was seen equatorward of the observatory, whereas eastward flow prevailed poleward. The reverse situation occurred in the corresponding (late evening) time sectors on the previous 3 nights we have presented, when the wind blew westward poleward of the observatory and eastward equatorward of the observatory. Presumably, the station passed under the equatorward edge of the late evening sunward flow on the 3 nights previously examined.

4.8. January 11, 1997

Figure 8 presents the clearest example we have of another type of spatial structure observed several times during the winter, that is, poleward flow near the midnight sector opposing the cross-polar jet. The data shown in Figure 8 were collected 1 day after the arrival at the Earth on January 10 of disturbed solar wind plasma associated (presumably) with a coronal mass ejection (CME) observed by the SOHO satellite beginning about 1600 UT on January 6. At the start of the period shown, the IMF was strongly northward (around +20 nT) and had been gradually building to this value over the previous 5 or 6 hours. The northward IMF began to weaken at around 0500 UT, so that by 0800 UT B_z was within a few nanoteslas of zero and remained thus for the rest of the night. Prior to 0800 UT the aurora lay poleward of the observatory; from 0800 to 1030 UT it lay roughly overhead; after a breakup at around 1030 UT it lay overhead or equatorward of the observatory until the end of the observations shown here.

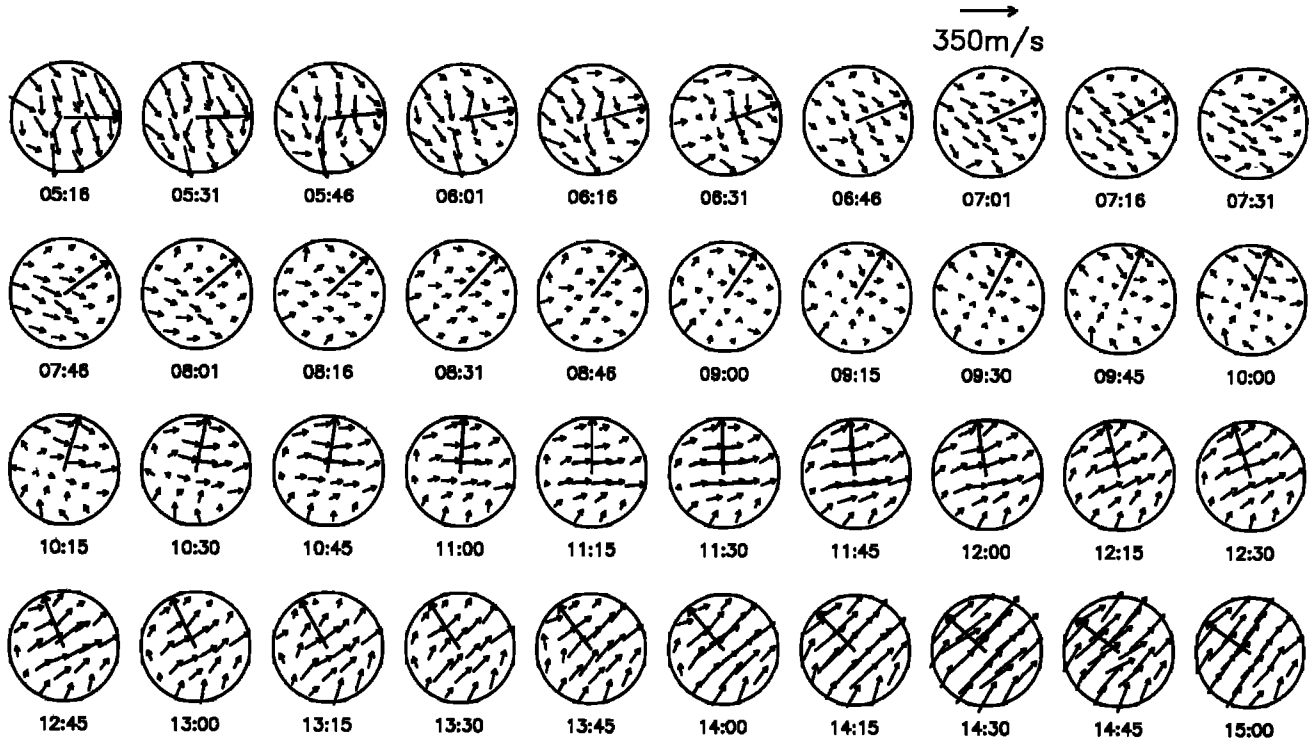

Figure 8. Evolution of the thermospheric horizontal vector wind field on the night of January 11, 1997.

Early in the evening the wind blew relatively uniformly antisunward. Over the next 4 hours the wind speed decreased and its direction rotated anticlockwise by almost 90°(seen in the Sun-aligned coordinates of Figure 8), although the wind never actually blew sunward. We assume these changes indicate the onset of weak ion drag forcing in opposition to the pressure gradient. It is not obvious when cross-polar jet first encountered the poleward edge of our field of view, but it was clearly present there by 0945 UT. Also by 0945 UT the wind equatorward of the observatory had begun to blow westward, resulting in a sheared flow similar in geometry to that which appeared about an hour earlier on the night of March 6, 1997. Unlike March 6, however, the westward flow equatorward of the observatory then turned poleward around 1030 UT, as if driven by a local pressure gradient associated with a heat source collocated with the breakup aurora. For the next hour or so, we observed colliding flows, with poleward wind originating equatorward of the observatory meeting the cross-polar jet and deflecting the jet eastward. These flows gradually merged, so that by 1215 UT the wind field began to look relatively uniform. This condition prevailed for the rest of the night. The resulting postmidnight flow was almost purely eastward, compared to the southeastward flow at this time on the previous days presented. Again, we understand this as a deflection of the cross-polar jet by a pressure gradient associated with auroral heating.

Poleward winds around magnetic midnight appeared relatively rarely in our observations, but this night was not an isolated example. Indeed, on the previous night (January 10), poleward winds were observed throughout the night from around 0500 UT onward. Between 1000 and 1400 UT the entire observable wind field blew uniformly poleward at around 200 $m\,s^{-1}$. The thermospheric circulation was unusual on January 10, 1997, a consequence of the arrival at Earth of the disturbed solar wind following the solar CME event on January 6. However, this does indicate that processes can occur at auroral latitudes which act to turn the wind poleward (and therefore sunward) even in the midnight sector.

5. Discussion

5.1. Comparison With Model Winds

Several of the properties of the winds that we have observed are unexpected, at least based on "generic" runs of thermospheric general circulation models. Figure 9 shows the output of the National Center for Atmospheric Research's Thermosphere, Ionosphere and Electrodynamics General Circulation Model (NCAR TIE-GCM), run for generic northern winter, solar minimum conditions. (The particular model run shown is identified in the output data file by the code "teesnd1.") The agreement between model and data is best early in the evening. The model plot for 0400 UT shows antisunward and slightly poleward winds over Alaska, blowing at about 120 $m\,s^{-1}$. This is consistent with almost all our observations at this universal time.

The model plot for 0800 UT shows westward wind over Alaska, as air parcels are carried by ion drag into

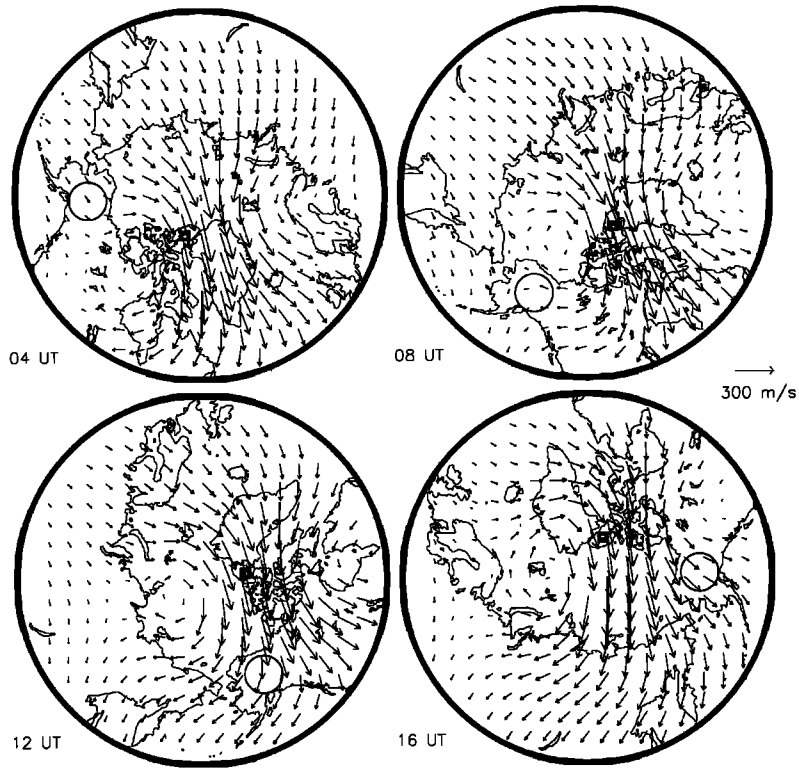

Figure 9. Output of the NCAR TIEGCM run for "generic" solar minimum, northern winter, magnetically quiet conditions. The model output data have been interpolated onto a surface of constant height at 250 km. Four universal times are shown. These are (clockwise from the top left): 0400, 0800, 1200, and 1600 UT. The local geographic noon meridian is at the top in each panel. The square west of northern Greenland indicates the ground level location of the north invariant pole taken from *Evans et al.* [1969]. The circle over Alaska shows the approximate field of view of our instrument.

the sunward eveningside flow. Our observations also frequently showed westward flow at this time. However, the model does not show the anticlockwise vorticity which we often observed along with the westward flow. Two examples of this vorticity are displayed here, in Figures 4 and 5. The model suggests that most of the air parcels that feed the sunward eveningside flow have come from the cross-polar jet and that there is almost no input of air from lower latitudes. By contrast, our data indicate that a substantial portion of the sunward flow may be drawn from the lower-latitude antisunward flow on the eveningside. Our observations do not preclude the possibility that some of the cross-polar jet air parcels do become entrained in the evening sector sunward flow. For example, this was clearly observed to occur between around 1016 and 1131 UT on March, 6, 1997. As a second example, the emerging cross-polar jet was also observed to turn westward and feed the sunward flow between about 0901 and 1001 UT on November 8, 1996. However, it was more common for us to observe flow configurations similar to Figures 4 and 5, with low-latitude air parcels feeding the sunward flow.

The emergence of the cross-polar jet on the nightside appears in the model as a very extensive feature covering 4 to 5 hours of local time. The depiction of the jet is not limited by the model's spatial resolution; the emergent jet is much larger than the model grid size. The model shows no sharp boundaries to the jet at auroral latitudes on the nightside. This is not what we observed. On each of the 5 days discussed in detail above, the cross-polar jet was observed to have a sharply defined edge, at least on its eveningside. At times, this edge was not resolved by our observations. That is, the transition to jet-dominated flow sometimes occurred within a distance spanned by only one of our observing zones. Since our zones project onto the thermosphere as regions of ~200 km spatial extent, we conclude that the eveningside edge of the cross polar-jet can span a distance of as little as 200 km, or less.

Often, but not always, we observed a period of weak and confused wind during the transition from late evening westward flow to postmidnight southeastward flow. We refer to this phenomenon as the premidnight doldrums. Again, the model winds in this time sector are dominated by the extensive emergence of the cross-polar jet and do not suggest that a region of "doldrums" above Alaska is likely in the 1-2 hours before magnetic midnight. One place where the model does predict doldrums followed by a sharp edge on the evening side of the cross-polar jet is where the jet flows past the stagnant region at the center of the model's dusk wind vor-

tex. However, the model's stagnant region lies a long way (~2000 km) sunward of Poker Flat at and before midnight. It would take a very severe distortion of the model to move this stagnant region over Poker Flat at, say, 1000 UT, in order to explain our observations of a wind abatement followed by the arrival of a sharply defined cross-polar jet.

The model plot for 1200 UT shows the cross-polar jet turning westward in the premidnight sector as it emerges on the nightside. This is the direction in which Coriolis acceleration would tend to turn it. As time advances, the model predicts that the wind over interior Alaska should blow magnetically southward or southwestward throughout the postmidnight period. For example, the plot for 1600 UT shows the wind blowing geographic southwestward so that, in a geomagnetic reference, it would blow south-southwestward. Again, this is not what we observed. Our first detections of the cross-polar jet occurred before magnetic midnight (which occurs at 1120 UT at Poker Flat). Usually, the jet was already flowing magnetically southeastward at that time, rather than in the southward or southwestward direction suggested by the model. Our postmidnight data are consistent with previously published FPS measurements of thermospheric winds above interior Alaska [e.g., *Hays et al.*, 1979; *Sica et al.*, 1989; *Smith et al.*, 1989], which all show magnetically southeastward wind after midnight. *Niciejewski et al.* [1996] also observed geomagnetically southeastward postmidnight flow at the relatively nearby site of Watson Lake, at least for observations around winter solstice time. (Their observations around equinox, in March of 1992 and of 1993, showed southward post-midnight winds.) While we continued to observe mostly southeastward postmidnight winds in all seasons, we did encounter some nights with southward or southwestward flow at this time and, indeed, these nights were also more prevalent in our data near equinox.

Since we have cautioned about the assumptions needed to infer vector wind fields from the line-of-sight data, it is worth considering how a breakdown of these assumptions may modify our model/data comparisons. We consider it unlikely that serious errors appear in the method's estimates of the uniform wind. Thus, neither our results showing southeastward postmidnight flow, nor those showing premidnight doldrums, are likely to be artifacts of our analysis. The assumptions in our analysis are needed to support our inferences of a sharply defined edge to the cross-polar jet and of a flow of low-latitude air parcels into the eveningside sunward wind. Thus these are our two observational results most needing further verification by an independent measurement technique.

Discrepancies between our inferred vector winds and the NCAR TIEGCM may all be related. Presumably, a process that created a sharp edge on the evening side of the cross-polar jet could also deflect it eastward and block the jet's natural tendency to turn westward due to the Coriolis force. By deflecting the emerging jet eastward, this same process could, at times, limit the recirculation of the jet into the evening sector sunward flow. With the jet prevented from spilling westward around midnight, this would allow the low-latitude pressure gradient wind to feed into the evening sector sunward flow on its equatorward side. When the doldrums are observed, it is usually shortly before midnight, in a local time sector where the model predicts south or southwestward flow at around 200 $\mathrm{m\,s^{-1}}$. We thus presume that the doldrums could result from the same process that deflected the jet eastward. Although we believe that a single process could account for all the observed discrepancies, the origin(s) of such a process remain unidentified.

5.2. Possible Reasons for Model/Data Discrepancies

Some empirical models of high-latitude ion convection, such as those of *Foster et al.* [1986], *Heppner and Maynard* [1987], or *Weimer* [1995], indicate that plasma emerging from the polar cap in the Harang discontinuity often has an eastward velocity component, particularly when the IMF B_z component is negative. This eastward component appears in these models for both positive and negative values of IMF B_y. The spatial extent of the region of eastward ion convection is such that an air parcel traveling at 150 to 200 $\mathrm{m\,s^{-1}}$ (typical of the velocities we observe in the cross-polar jet) would take an hour or more to cross it. This time is comparable to the time constant for ion-neutral momentum coupling. Thus the direction of emergence of the air parcels from the neutral cross-polar jet could arise either because ion drag in the Harang discontinuity was actually directed more strongly eastward than was assumed in the model, or because the ion-neutral momentum coupling was stronger than assumed in the model.

Unfortunately, not all ionospheric convection models show such consistent eastward flow in the Harang discontinuity. For example, for IMF B_z negative and B_y positive, the Harang discontinuity depicted in the model of *Hairston and Heelis* [1990] does not contain strongly eastward plasma flow at the latitude of Poker Flat. It is therefore difficult to know how probable the above described eastward deflection by ion drag is in practice.

Another possibility is that a process (which is currently poorly described by the model) occurs in the night side auroral zone and acts to oppose the emergence of the cross-polar jet from the nightside polar cap. For example, *Heppner and Miller* [1982] described observations of deceleration of the cross-polar jet as it crossed the auroral zone on the nightside, based on nine upleg/downleg chemical release rocket flights. Eight of these flights showed wind velocities that were higher at the poleward release location than at the equatorward location. For the ninth flight, there was almost no difference. Based on these flights, they estimated that the rate of retardation of the jet was approximately 40 $\mathrm{m\,s^{-1}}$per degree of magnetic latitude, at a height of 230 km. Since our field of view spans approximately 9° of latitude, their estimated rate of retardation would be sufficient to stop a 150 $\mathrm{m\,s^{-1}}$ cross-polar jet after crossing only 40% of our field of view (assuming a constant

retardation). Such a retardation rate is of the right order of magnitude to be consistent with our observations of a sharp edge on the cross-polar jet, and of the doldrums phenomenon.

The auroral oval is known to be collocated with regions of elevated Joule heating, auroral particle heating, and ionospheric electrical conductivity [e.g., *Ahn et al.* 1983a, b, 1989; *Foster et al.*, 1983, 1986; *Kamide and Kroehl*, 1987; *Rich et al.*, 1987; *Richmond*, 1992; *Lu et al.*, 1995; *Thayer et al.*, 1995; *Lummerzheim et al.*, 1997]. Both Joule and particle heating deposit most energy per unit volume at altitudes below the ~240 km height that we observed [e.g., *Banks*, 1977; *Brekke and Rino*, 1978; *Rees et al.*, 1983]. When expressed per unit mass, the particle heat deposition should be approximately constant with altitude in the thermosphere, and Joule heating may actually maximize near or even above our observing height [*Millward et al.*, 1993; *Fujiwara et al.*, 1996].

We may thus expect that the thermosphere above Poker Flat would routinely exhibit upward vertical wind as it crosses the auroral zone each night. Prior observations of vertical winds do indeed suggest that the nightside auroral oval is a region of enhanced vertical circulation [*Spencer et al.*, 1982; *Wardill and Jacka*, 1986; *Crickmore et al.*, 1991; *Eastes et al.*, 1992; *Price et al.*, 1995; *Innis et al.*, 1996, 1997]. The *Price et al.* [1995] and *Innis et al.* [1996, 1997] studies further indicated that a region of upwelling spanning around 400 km in latitude lies slightly poleward of the nightside discrete aurora, whereas the *Crickmore et al.* [1991] study suggested that downwelling occurs near the equatorward edge of the auroral oval. *Innis et al.* [1997] showed that the occurrence of upwelling above Mawson, Antarctica, maximized during the 3 to 4 hours either side of local magnetic midnight, whereas downwelling was most frequent over an ~8 hour period centered ~8 hours prior to magnetic midnight. Because Mawson typically lies equatorward of the oval early in the evening, but passes under it prior to magnetic midnight, these times are consistent with the picture of upwelling poleward of the oval and downwelling equatorward of it.

Rishbeth et al. [1987, and other references cited therein] have pointed out that vertical winds may be considered as consisting of two components. These are the "barometric" component due to the rise and fall of fixed pressure levels as the thermosphere expands or contracts in response to heating or cooling and the "divergence" component driven by the requirement to maintain mass continuity in the presence of horizontal convergence or divergence. The divergence component provides a coupling between horizontal and vertical winds and can act either to drive vertical winds or to limit them. For example, a convergent horizontal wind may drive an upward wind, whereas an upward wind driven from below will produce horizontal divergence at greater altitudes, which acts to limit the otherwise exponential increase of V_z with height required by mass continuity.

Various modeling studies of the thermospheric response to impulsive increases in geomagnetic heating suggest that the "divergence" component of the vertical wind can drive divergent horizontal meridional winds at 240 km altitude to velocities of at least 100 $\mathrm{m\,s^{-1}}$, and possibly much more [*Fuller-Rowell*, 1984, 1985; *Walterscheid and Boucher*, 1984; *Chang and St.-Maurice*, 1991; *Millward et al.*, 1993; *Fujiwara et al.*, 1996]. These velocities are comparable to the ~150 $\mathrm{m\,s^{-1}}$ that we observe at solar minimum in the cross-polar jet as it emerges from the polar cap on the nightside. Thus meridional divergence associated with upward winds driven by an auroral heat source could act poleward of the upwelling to deflect the cross-polar jet. During the time period between about 1015 and 1200 UT shown in Figure 8, we observed exactly the flow configuration expected if this process were occurring.

We have seen similar poleward flows in the evening and midnight sectors on other days as well. Figure 7 shows poleward flow in the late evening, between about 0701 and 0816 UT. Although not shown here, the night of January 10, 1997, was another example. Interestingly, although we postulate that the poleward flow seen between about 1015 and 1200 UT in Figure 8 was driven by divergence of an upward wind somewhere equatorward of our observatory, the wind field that we actually observed was convergent, as poleward flow collided with the cross-polar jet. Although we cannot tell what vertical wind was associated with this convergence, one possibility is that it drove downwelling, and so provided the return path to complete a convective circulation cell, originally established by the postulated auroral heating lying equatorward of us.

Horizontal divergence associated with upwelling in the local time sector between 2000 to 0400 hours magnetic local time thus appears likely to play some role in the observed eastward deflection of the cross-polar jet. "Statistical" auroral ovals suggest that an upwelling region poleward of the discrete aurora would be expected to lie poleward of our observatory before midnight. The poleward part of a meridionally divergent upwelling could still deflect the jet eastward. However, in this case we would also expect to see the corresponding equatorward component of the divergence appearing above our observatory, in contrast to the observations, which do not show this. That is, we did not usually see a strong equatorward wind in the premidnight sector. The meridian scanning photometer (MSP) and all-sky camera frequently showed that breakup aurora actually lay overhead or even equatorward of Poker Flat in the late evening and onward (rather than poleward, as expected statistically). For example, see Figure 10 showing the MSP record for November 15, 1996. Breakup aurora was observed overhead after about 1000 UT. This time corresponds closely to the onset of the "doldrums" in the FPS data shown in Figure 4. Between 1300 and 1400 UT, the aurora lay equatorward of Poker Flat.

A vertical wind also acts to advect horizontal momentum. Rocket-borne chemical release measurements of neutral winds in the 100-250 km altitude range indicate that the wind speed frequently decreases with decreasing height between 250 km and about 140 km

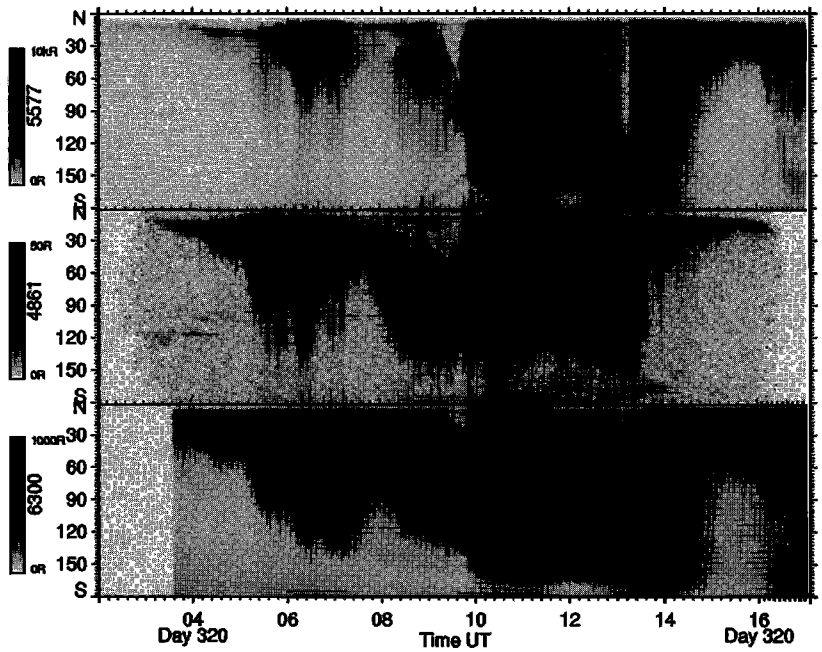

Figure 10. Poker Flat meridian scanning photometer data for November 15, 1996. These panels indicate airglow and auroral emission intensities at (top) λ557.7 nm, (middle) λ486.1 nm, and (bottom) λ630.0 nm measured along the magnetic meridian as functions of universal time. The Y axis indicates viewing angle in degrees along the magnetic meridian, with 0 corresponding to the north horizon and 180 to the south horizon. The intensity scale is linear, with black corresponding intensities of at least 10000, 50, and 1000 Rayleighs for the top, middle and bottom panels, repectively.

(below 140 km isolated high-velocity jets are sometimes observed) [*Heppner and Miller*, 1982; *Mikkelsen et al.*, 1987; *Larsen and Mikkelsen*, 1990; *Larsen et al.*, 1995]. If the wind speed decreases with decreasing height, air parcels lifted aloft will be moving at smaller horizontal velocities than the air parcels they displace. The process can be visualized by imagining (relatively) dense and stagnant air parcels being lifted upward from around 140 km, expanding horizontally as they rise, and producing a plume of air which is upward flowing but horizontally sluggish (i.e., sluggish compared to typical F region wind speeds). If such an upwelling plume of sluggish air does exist at 240 km altitude, the previously cited vertical wind studies suggest it would be ~400 km wide latitudinally but extended over perhaps 6 hours in local time and that it would lie slightly poleward of the auroral oval. We therefore picture the cross-polar jet emerging from the polar cap and "running into" a barrier of slowly moving air. Such a process could explain the sharp edge of the jet, its eastward deflection, and the premidnight doldrums.

Heppner and Miller [1982, p1645] reported an anomalous rocket flight, launched from Poker Flat at 1426 UT on March 7, 1972, in which abnormally low wind velocities ($\prec$ 60 ms^{-1}) were observed at all altitudes above 160 km (up to 290 km). Kp was 4+ at the time of the flight. They described the launch as occurring "several hours after a period of many hours of intense substorm activity" and speculated that the associated prolonged thermospheric heating may have produced stagnant winds, rather than the more typically expected increase in wind speeds. They also noted that simultaneously released ion clouds did not show any abnormality in the electric field at this time. To explain these (very direct) observations, a mechanism is needed which could retard the wind at all heights above 160 km, yet acts purely through neutral dynamics, that is, without invoking exotic electric fields and associated ion drag forcing. Vertical advection of horizontal momentum could do this. The preceding active aurora indicates that E region heating had been occurring, suggesting that conditions were indeed favorable to drive such vertical advection.

Millward et al. [1993] performed a simulation study of a short-lived (~10 min) but very intense enhancement of the high-latitude convection electric field and Joule heating during solar maximum winter conditions. For the disturbance they simulated, the vertical velocities above the heat source at an altitude of around 280 km maximized about 4 minutes after the onset of heating, at ~170 ms^{-1}. They performed an analysis of the forcing terms responsible for the subsequent thermospheric response and found that at 280 km the horizontal acceleration due to vertical advection of momentum peaked about 12 min after the heating onset, at around -0.3 ms^{-2}. The negative sign here indicates that vertical advection of momentum acted to decelerate the wind at this height. The value of -0.3 ms^{-2} is a very large acceleration term, as can be seen by comparison of this with the results of *Killeen and Roble* [1984], who performed

a force analysis of the steady state wind field generated by the NCAR Thermospheric General Circulation Model (TGCM) for solar maximum winter conditions. They found that at around 300 km in the midnight sector the steady-state force per unit mass balance was dominated by the ion drag, Coriolis, and pressure gradient terms, all of which had comparable magnitudes in the approximate range 0.03 to 0.07 ms^{-2}. These three forces were in approximate balance, and so summed to a value of $\sim$0.02 ms^{-2}, or less.

The degree of electric field enhancement used in the simulation of *Millward et al.* [1993] generated a very large upward wind. The peak value of $\sim$170 ms^{-1} should be compared with the results of *Conde and Dyson* [1995b], who found that the $1/e$ half width of the distribution of vertical velocities within a set of 2096 vertical wind measurements from the auroral zone site of Mawson, Antarctica, was only 16 ms^{-1}. The *Conde and Dyson* [1995b] result was representative of vertical winds from all observations taken in a 7 month period and would clearly underestimate the typical vertical velocities expected solely within the postulated region of upwelling at the poleward edge of the nightside discrete aurora. In any case, even if the *Millward et al.* [1993] model overestimated the acceleration due to vertical advection of horizontal momentum in the upwelling region by a factor of 4, this term would still exceed the expected values of each of the other forces driving the wind and easily exceed the sum of these other forces.

An air parcel originating in the cross-polar jet with an initial speed of 150 ms^{-1} would be slowed to a halt within half an hour by a uniform deceleration of 0.075 ms^{-2} (25% of the advective deceleration associated with the event simulated by *Millward et al.* [1993]). Over this time it would travel only 150 km, a distance smaller that the expected width of the upward plume, but comparable to width of the "edge" we have observed on the cross-polar jet. Vertical advection of horizontal momentum in the real atmosphere is obviously unlikely to produce such a simple, uniform, deceleration. Nevertheless, this calculation does suggest that vertical advection may indeed be strong enough and spatially extended enough to retard or deflect the cross-polar jet as it emerges from the polar cap. In so doing it could reshape the high-latitude thermospheric horizontal circulation throughout the entire dusk-to-postmidnight sector.

In seeking to understand why our experimental results do not match the model, we need to find processes that could occur in the real atmosphere but which are either nonexistent or poorly described in the model. Both of the suggested mechanisms for retarding the cross-polar jet as it crosses the auroral zone (i.e., divergence and vertical advection) are driven by vertical winds associated with the aurora. Since these vertical winds are expected to occur in a latitudinally narrow band, they may not be well modeled by the TIEGCM. The TIEGCM horizontal grid size is $5° \times 5°$, which means that it would have at most one grid point within the expected latitudinal zone of upwelling.

As noted in our section on wind vector estimation, this experiment also yielded observations of vertical wind velocities. We therefore examined the vertical wind data for evidence of either of the associations between horizontal and vertical winds that we have proposed above. We did not find any significant, systematic relations between our vertical and horizontal wind observations. There are several possible reasons for this. First, our integration times in this experiment were chosen to yield typical wind uncertainties of around 20 ms^{-1}. This is adequate for measuring F region horizontal winds, which typically exceed 100 ms^{-1}, but it is marginal at best for vertical wind measurements. Second, both the processes of horizontal divergence and of vertical advection of momentum would be expected to have most impact on the horizontal wind at 240 km in regions displaced horizontally by up to several hundred kilometers away from the original upwelling. Thus it is unlikely that a single instrument would simultaneously observe both the effects of these mechanisms and the upward wind which acted as their source. (Recall that our instrument can only measure vertical wind in a small region centered on the zenith.) Third, as pointed out by *Innis et al.* [1996, 1997], our geomagnetic latitude of 65° is such that if the upwelling were observable in our zenith at or before midnight, then the latitude of the auroral oval would tend to be less stable than at times when the oval is more contracted. Thus the conditions needed to make the upwelling observable to us would also make that observability transient, especially compared to our 15 min integration times. To test adequately for evidence of either of the proposed processes relating vertical and horizontal wind fields would require (say) two more FPIs dedicated to zenith-pointing vertical wind measurements. These instruments would need to be sited several hundred kilometers north and south of our existing instrument, and all three instruments would need to make simultaneous observations.

5.3. The Significance of Observing at Solar Minimum

To date, our only observations using the present instrument have been at solar minimum. As it happens, most prior measurements of thermospheric winds from near our location (cited previously) have been gathered close to solar maximum. Many of these prior observations do show magnetically southeastward winds in the postmidnight sector. However, "premidnight doldrums" winds do not appear often in the prior measurements. *Heppner and Miller* [1982] did report one nightside rocket flight near solar maximum (discussed previously) showing "anomalous" light winds above 160 km, although this flight was launched later in the evening than when we typically saw wind doldrums. Wind averages presented by *Niciejewski et al.* [1996] based on observations between December 1991 and March 1993 contain several periods which may correspond to the doldrums phenomenon, even in the averages. However, solar activity declined in the 1991 to 1993 period, so these results do not truly represent solar maximum. The pre-

viously cited Fabry-Perot observations from near Poker Flat used narrow-field instruments sampling in only four directions. In such cases, wind vectors must be constructed by temporal interpolation of line-of-sight measurements in each direction. It is possible that this interpolation would "fill in" the doldrums period with smoothly varying winds, based on values before and after the doldrums. Any such effect could be enhanced by averaging multiple days. As a result, the previously published solar maximum wind averages may not resolve the relatively brief period of doldrums that we observe on individual days, and thus give the impression that doldrums do not occur at solar maximum.

We also considered the possibility that, near solar maximum, the cross-polar jet is not strongly affected by its passage through the nightside auroral zone. For example, a fast flowing jet would presumably be less influenced by local vertical winds in the auroral zone than a slow flowing jet. Indeed, thermospheric wind observations by *Aruliah et al.* [1991a, b] from the auroral latitude site of Kiruna, Sweden, indicated that for $Kp \succ 5$ the cross-polar jet speed doubled between solar minimum and solar maximum. However, the variation was small under magnetically quiet conditions. This is consistent with the result of *Wickwar et al.* [1984] who found "no discernible effects" on the meridional wind above Poker Flat due to solar cycle variations. Generally, prior observations do not indicate that the cross-polar jet flows significantly faster during solar maximum than it does at solar minimum, at least for magnetically quiet conditions (typical of the days we have presented here). A final possibility is that elevated F region electron densities at solar maximum may allow ion drag to drive the cross-polar jet across the nightside auroral zone more effectively than it could at solar minimum, thus making the onset of doldrums less likely. Since we do not have ready access to ionospheric data for the previously published study periods, we have not attempted to test this hypothesis.

5.4. Day-to-Day Variability of the Observed Winds

As a final comment, it is clear from our observations that although similar features were observed in the wind on many days, the details of their appearance were subject to significant day-to-day variability. For example, although we may recognize the signature of ion drag driving the wind sunward in the late evenings of many observing periods, the intensities, local times, and latitudes of occurrence of sunward flow could vary substantially. We expect that geophysical indices describing quantities with planet-wide impact, such as Kp, $F_{10.7}$, IMF values, or solar wind parameters, would be of limited value for predicting these details (although all certainly are needed to predict the large-scale wind circulation). Rather, it is our impression that a successful high-resolution regional wind model would also need inputs containing high-resolution observations of processes that determine the local forcing over horizontal length scales of several hundred kilometers, or less. Key parameters to image would be the auroral precipitation, plasma convection, and ionospheric electron density. Thus there is a strong future incentive to cluster instruments with these measurement capabilities alongside a wind imaging instrument.

6. Conclusions

The wavelength-scanning, all-sky imaging Fabry Perot spectrometer has allowed us to infer the time evolution of spatial variations in thermospheric horizontal winds over a geographic region roughly 1000 km in diameter. This is a new technique, as yet unvalidated by comparison with other methods. Until such methods are available, the results presented here should be regarded as preliminary.

Examples of our inferred vector wind fields from six observing nights have been presented. Line-of-sight wind data from five of these nights suggested that spatially structured thermospheric winds occurred within our field of view. Data from the sixth, presented for comparison, indicated relatively uniform (but still time varying) winds throughout the night. The occurrence of spatially structured wind fields appeared to arise mainly from the superposition of ion drag forcing upon the otherwise slowly varying pressure gradient driven wind. The precise details of the atmospheric response to these competing process varied from day to day.

Our results have been compared with NCAR's TIE-GCM thermospheric model. While agreement was good at the beginning and the end of the night, the modeled wind patterns did not agree with our inferred vector fields in the late evening and midnight sectors. The model suggests that sunward flow on the eveningside is fed almost exclusively from a westward turning of the cross-polar jet as it emerges on the nightside of the polar cap. Our results indicate that, at least at solar minimum, the cross-polar jet generally does not turn westward as it emerges and thus can only supply air parcels to the poleward side of the sunward evening flow. Our results further suggest that there can be a significant feed of air parcels from the low-latitude pressure gradient flow into the evening sunward flow. These parcels would enter the sunward flow on its equatorward side. There appeared to be a sharp boundary on the eveningside of the cross-polar jet at our latitude, often preceded by a period of weak and confused thermospheric winds.

We have discussed several processes which may account for the differences between our inferred vector wind fields and the model. Ion convection in the Harang discontinuity may actually have been directed more eastward during our observations than was assumed by the model, or the ion-neutral momentum coupling may have been stronger there. Vertical winds driven by auroral heating could deflect the emergence of the cross-polar jet from the nightside polar cap, either by establishing meridionally divergent horizontal winds, or through the vertical advection of horizontal momentum. Of course, our results may indicate that more than one of these processes was occurring, and possibly all three.

Acknowledgments. This work was supported by NSF grant ATM-9523810. NCAR TIEGCM data were kindly provided by Raymond Roble and Ben Foster. We thank June Pelehowski for supporting the operation of the Fabry-Perot spectrometer, meridian scanning photometer, and the observatory at Poker Flat.

The Editor thanks G. G. Shepherd and another referee for their assistance in evaluating this paper.

References

Ahn, B.-H., S. I. Akasofu, and Y. Kamide, The joule heat production rate and the particle energy injection rate as a function of the geomagnetic indices AE and AL, *J. Geophys. Res.,88*, 6275-6287, 1983a.

Ahn, B.-H., R. M. Robinson, Y. Kamide, and S. I. Akasofu, Electric conductivities, electric fields and auroral particle energy injection rate in the auroral ionosphere and their empirical relations to the horizontal magnetic disturbances, *J. Geophys. Res.,88*, 641-653, 1983b.

Ahn, B.-H., H. W. Kroehl, Y. Kamide, D. J. Gorney, S.-I. Akasofu, and J. R. Kan, The auroral energy deposition over the polar ionosphere during substorms, *Planet. Space Sci.,37*, 239-252, 1989.

Aruliah, A. L., D. Rees, and T. J. Fuller-Rowell, The combined effect of solar and geomagnetic activity on high latitude thermospheric neutral winds, I, Observations, *J. Atmos. Terr. Phys.,53*(6-7), 467-483, 1991a.

Aruliah, A. L., D. Rees, and A. Steen, Seasonal and solar cycle variations in high-latitude thermospheric winds, *Geophys. Res. Lett.,18*, 1983-1986, 1991b.

Banks, P. M., Observations of Joule and particle heating in the auroral zone, *J. Atmos. Terr. Phys.,39*, 179-193, 1977.

Bates, H. F., and T. D. Roberts, The southward midnight surge in *F*- layer wind observed with the Chatanika incoherent scatter radar, *J. Atmos. Terr. Phys.,39*, 87-93, 1977.

Batten, S., and D. Rees, Thermospheric winds in the auroral oval: Observations of small scale structures and rapid fluctuations by a Doppler imaging system, *Planet. Space Sci.,38*, 675-694, 1990.

Batten, S., D. Rees, D. Wade, and A. Steen, Observations of thermospheric neutral winds by the UCL Doppler imaging system at Kiruna in northern Scandinavia, *J. Atmos. Terr. Phys.,50*, 861-888, 1988.

Biondi, M. A., D. P. Sipler, M. E. Zipf, and J. L. Baumgardner, All-sky Doppler interferometer for thermospheric dynamics studies, *Appl. Opt., 34*, 1646-1654, 1995.

Brekke, A., and C. L. Rino, High-resolution altitude profiles of the auroral zone energy dissipation due to ionospheric currents, *J. Geophys. Res.,83*, 2517-2524, 1978.

Browning, K. A., and R. Wexler, The determination of kinematic properties of a wind field using Doppler radar, *J. App. Meteorol.,7*, 105-113, 1968.

Burnside, R. G., F. A. Herrero, J. W. Meriwether Jr., and J. C. G. Walker, Optical observations of thermospheric dynamics at Arecibo, *J. Geophys. Res.,86*, 5532-5540, 1981.

Chang, C. A., and J.-P. St.-Maurice, Two-dimensional high-latitude thermospheric modeling: A comparison between moderate and extremely disturbed conditions, *Can. J. Phys.,69*, 1007-1031, 1991.

Conde, M., and P. L. Dyson, Thermospheric horizontal winds above Mawson, Antarctica, *Adv. Space Res.,16*, 41-52, 1995a.

Conde, M., and P. L. Dyson, Thermospheric vertical winds above Mawson, Antarctica, *J. Atmos. Terr. Phys.,57*, 589-596, 1995b.

Conde, M., and R. W. Smith, Mapping thermospheric winds in the auroral zone, *Geophys. Res. Lett.,22*, 3019-3022, 1995.

Conde, M., and R. W. Smith, "Phase compensation" of a separation scanned, all-sky imaging Fabry-Perot spectrometer for auroral studies, *Appl. Opt.,36*, 5441-5450, 1997.

Crickmore, R. I., J. R. Dudeney, and A. S. Rodger, Vertical thermospheric winds at the equatorward edge of the auroral oval, *J. Atmos. Terr. Phys.,53*(6-7), 485-492, 1991.

Eastes, R. W., T. L. Killeen, Q. Wu, J. D. Winningham, W. R. Hoegy, L. E. Wharton, and G. R. Carignan, An experimental investigation of thermospheric structure near an auroral arc, *J. Geophys. Res.,97*, 10539-10549, 1992.

Evans, J. E., L. L. Newkirk, and B. M. McCormac, *North polar, south polar, world maps and tables of invariant magnetic coordinates for six altitudes: 0, 100, 300, 600, 1000, and 3000 KM, DASA 2347*, Lockheed Palo Alto Res. Lab., Palo Alto, Calif., 1969.

Foster, J. C., J. P. St. Maurice, and V. J. Abreu, Joule heating at high latitudes, *J. Geophys. Res.,88*, 4885-4896, 1983.

Foster, J. C., J. M. Holt, R. G. Musgrove, and D. S. Evans, Solar wind dependencies of high-latitude convection and precipitation, in *Solar Wind-Magnetosphere Coupling* , edited by Y. Kamide and J. A. Slavin, pp. 477-494, Terra Sci., Tokyo, 1986.

Fujiwara, H., S. Maeda, H. Fukunishi, T. J. Fuller-Rowell, and D. S. Evans, Global variations of thermospheric winds and temperatures caused by substorm energy injection, *J. Geophys. Res.,101*, 225-239, 1996.

Fuller-Rowell, T. J., A two-dimensional, high-resolution, nested-grid model of the thermosphere, 1, Neutral response to an electric field "spike," *J. Geophys. Res., 89*, 2971-2990, 1984.

Fuller-Rowell, T. J., A two-dimensional, high-resolution, nested-grid model of the thermosphere, 2, Response of the thermosphere to narrow and broad electrodynamic features, *J. Geophys. Res.,90*, 6567-6586, 1985.

Hairston, M. R., and R. A. Heelis, Model of the high-latitude ionospheric convection pattern during southward interplanetary magnetic field using DE 2 data, *J. Geophys. Res.,95*, 2333-2343, 1990.

Hays, P. B., J. W. Meriwether Jr., and R. G. Roble, Nighttime thermospheric winds at high latitudes, *J. Geophys. Res.,84*, 1905- 1913, 1979.

Hays, P. B., T. L. Killeen, N. W. Spencer, L. E. Wharton, R. G. Roble, B. A. Emery, T. J. Fuller-Rowell, D. Rees, L. A. Frank, and J. D. Craven, Observations of the dynamics of the polar thermosphere, *J. Geophys. Res.,89*, 5597-5612, 1984.

Heppner, J. P., and N. C. Maynard, Empirical high latitude electric field models, *J. Geophys. Res.,92*, 4467-4489, 1987.

Heppner, J. P., and M. L. Miller, Thermospheric winds at high latitudes from chemical release observations, *J. Geophys. Res.,87*, 1633-1647, 1982.

Innis, J. L., P. A. Greet, and P. L. Dyson, Fabry-Perot spectrometer observations of the auroral oval/polar cap boundary above Mawson, Antarctica, *J. Atmos. Terr. Phys.,58*, 1973-1988, 1996.

Innis, J. L., P. L. Dyson, and P. A. Greet, Further observations of the thermospheric vertical wind at the auroral oval/polar cap boundary above Mawson station, Antarctica, *J. Atmos. Terr. Phys.,59*, 2009-2022, 1997.

Ishii, M., S. Okano, E. Sagawa, S. Watari, H. Mori, I. Iwamoto, and Y. Murayama, Development of Fabry-Perot interferometers for airglow observations, *Proc. NIPR Symp. Upper Atmos. Phys.,10*, 97-108, 1997.

Kamide, Y., and H. W. Kroehl, A concise review of the utility of ground based magnetic recordings for estimating the Joule heat production rate, *Ann. Geophys.*,*5*, 535-542, 1987.

Keskinen, M. J., and P. Satyanarayana, Nonlinear unstable auroral-arc driven thermospheric winds in an ionosphere-magnetosphere coupled model, *Geophys. Res. Lett.*,*20*, 2687-2690, 1993.

Killeen, T. L., and R. G. Roble, An analysis of the high latitude thermospheric wind pattern calculated by a thermospheric general circulation model: 1. Momentum forcing, *J. Geophys. Res.*,*89*, 7509-7522, 1984.

Killeen, T. L., and R. G. Roble, Thermosphere dynamics: Contributions from the first 5 years of the Dynamics Explorer program, *Rev. Geophys.*, *26*, 329-367, 1988.

Killeen, T. L., P. B. Hays, G. R. Carnigan, R. A. Heelis, W. B. Hanson, N. W. Spenser, and L. H. Brace, Ion-neutral coupling in the high latitude f region: Evaluation of the ion heating terms from dynamics explorer 2, *J. Geophys. Res.*,*89*, 7495-7508, 1984.

Killeen, T. L., J. D. Craven, L. A. Frank, J. J. Ponthieu, N. W. Spencer, R. A. Heelis, L. H. Brace, R. G. Roble, P. B. Hays, and G. R. Carnigan, On the relationship between dynamics of the polar thermosphere and morphology of the aurora: Global-scale observations from Dynamics Explorers 1 and 2, *J. Geophys. Res.*,*93*, 2675-2692, 1988.

Larsen, M. F., and I. S. Mikkelsen, Vertical velocities and momentum fluxes derived from wind measurements in the dusk auroral oval, *J. Geophys. Res.*,*95*, 21051-21057, 1990.

Larsen, M. F., T. R. Marshall, I. S. Mikkelsen, B. A. Emery, A. Christensen, D. Kayser, J. Hecht, L. Lyons, and R. Walterscheid, Atmospheric Response in Aurora experiment: Observations of E and F region neutral winds in a region of postmidnight diffuse aurora, *J. Geophys. Res.*,*100*, 17299-17308, 1995.

Larsen, M. F., A. B. Christensen, and C. D. Odom, Development of unstable atmospheric layers near 100 km in the postmidnight auroral oval, *Geophys. Res. Lett.*,*24*, 1915-1918, 1997.

Lu, G., A. D. Richmond, B. A. Emery, and R. G. Roble, Magnetosphere- ionosphere-thermosphere coupling: Effect of neutral winds on energy transfer and field-aligned current, *J. Geophys. Res.*,*100*, 19643-19659, 1995.

Lummerzheim, D., M. Brittnacher, D. Evans, G. A. Germany, G. K. Parks, M. H. Rees, and J. F. Spann, High time resolution study of the hemispheric power carried by energetic electrons into the ionosphere during the May 19/20, 1996 auroral activity, *Geophys. Res. Lett.*,*24*, 987-990, 1997.

Lyons, L. R., and R. L. Walterscheid, Generation of auroral omega bands by shear instability of the neutral winds, *J. Geophys. Res.*,*90*, 12321-12329, 1985.

McCormac, F. G., and R. W. Smith, The influence of the interplanetary magnetic field Y component on ion and neutral motions in the polar thermosphere, *Geophys. Res. Lett.*,*11*, 935-938, 1984.

McCormac, F. G., T. L. Killeen, and J. P. Thayer, The influence of IMF B_Y on the high latitude thermospheric circulation during northward IMF, *J. Geophys. Res.*,*96*, 115-128, 1991.

Meriwether, J. W., Jr., J. P. Heppner, J. D. Stolarik, and E. M. Wescott, Neutral winds above 200 km at high latitudes, *J. Geophys. Res.*, *78*, 6643-6661, 1973.

Meriwether, J. W., Jr., T. L. Killeen, F. G. McCormac, A. G. Burns, and R. G. Roble, Thermospheric winds in the geomagnetic polar cap for solar minimum conditions, *J. Geophys. Res.*,*93*, 7478-7492, 1988.

Mikkelsen, I. S., T. S. Jorgensen, M. C. Kelley, M. F. Larsen, E. Pereira, and J. Vickrey, Neutral winds and electric fields in the dusk auroral oval 1. measurements, *J. Geophys. Res.*,*86*, 1513-1524, 1981.

Mikkelsen, I. S., M. F. Larsen, M. C. Kelley, J. Vickrey, E. Friis-Christensen, J. Meriwether, and P. Shih, Simultaneous measurements of the thermospheric wind profile at three separate positions in the dusk auroral oval, *J. Geophys. Res.*,*92*, 4639-4648, 1987.

Millward, G. H., S. Quegan, R. J. Moffett, T. J. Fuller-Rowell, and D. Rees, A modelling study of the coupled ionospheric and thermospheric response to an enhanced high-latitude electric field event, *Planet. Space Sci.*,*41*(1), 45-56, 1993.

Nagy, A. F., R. J. Cicerone, P. B. Hays, K. D. McWatters, J. W. Meriwether Jr., A. E. Belon, and C. L. Rino, Simultaneous measurements of ion and neutral motions by radar and optical techniques, *Radio Sci.*,*9*, 315-321, 1974.

Nakajima, H., S. Okano, H. Fukunishi, and T. Ono, Observations of thermospheric wind velocities and temperatures by use of a Fabry-Perot Doppler imaging system at Syowa Station, Antarctica, *Appl. Opt.*,*34*, 8382-8395, 1995.

Niciejewski, R. J., T. L. Killeen, and S. C. Solomon, Observations of thermospheric horizontal winds at Watson Lake, Yukon Territory (Λ = 65N), *J. Geophys. Res.*,*101*, 241-259, 1996.

Price, G. D., and F. Jacka, The influence of geomagnetic activity on the upper mesosphere/lower thermosphere in the auroral zone, I, Vertical winds, *J. Atmos. Terr. Phys.*,*53*, 909-922, 1991.

Price, G. D., R. W. Smith, and G. Hernandez, Simultaneous measurements of large vertical winds in the upper and lower thermosphere, *J. Atmos. Terr. Phys.*,*57*, 631-643, 1995.

Rees, D., and A. H. Greenaway, Doppler imaging system; an optical device for measuring vector winds, 1, General principles, *Appl. Opt.*,*22*, 1078-1083, 1983.

Rees, D., A. H. Greenaway, R. Gordon, I. McWhirter, P. J. Charleton, and A. Steen, The Doppler imaging system: initial observations of the auroral thermosphere, *Planet. Space Sci.*,*32*, 273-285, 1984a.

Rees, D., R. W. Smith, P. J. Charleton, F. G. McCormac, N. LLoyd, and A. Steen, The generation of vertical thermospheric winds and gravity waves at auroral latitudes, I, Observations of vertical winds, *Planet. Space Sci.*, *32*, 667-684, 1984b.

Rees, M. H., B. A. Emery, R. G. Roble, and K. Stamnes, Neutral and ion gas heating by auroral electron precipitation, *J. Geophys. Res.*,*88*, 6289-6300, 1983.

Rich, F. J., M. S. Gussenhoven, and M. E. Greenspan, Using simultaneous particle and field observations on a low altitude satellite to estimate Joule heat energy flow into the high latitude ionosphere, *Ann. Geophys.*,*5*, 527-534, 1987.

Richmond, A. D., Assimilative mapping of ionospheric electrodynamics, *Adv. Space Res.*,*6*, 59-68, 1992.

Rishbeth, H., T. J. Fuller-Rowell, and D. Rees, Diffusive equilibrium and vertical motion in the thermosphere during a severe magnetic storm: A computational study, *Planet. Space Sci.*,*35*, 1157-1165, 1987.

Sekar, R., S. Gurubaran, and R. Sridharan, All sky imaging Fabry-Perot spectrometer for optical investigation of the upper atmosphere, *Indian J. Rad. Space Phys.*,*22*, 197-204, 1993.

Sica, R. J., M. H. Rees, G. J. Romick, G. Hernandez, and R. G. Roble, Auroral zone thermospheric dynamics, 1, Averages, *J. Geophys. Res.*,*91*, 3231-3244, 1986.

Sica, R. J., G. Hernandez, B. A. Emery, R. G. Roble, R. W.

Smith, and M. H. Rees, The control of auroral zone dynamics and thermodynamics by the interplanetary magnetic field dawn-dusk (Y) component, *J. Geophys. Res.*, *94*, 11921-11932, 1989.

Sica, R. J., J.-P. St.-Maurice, G. Hernandez, G. J. Romick, and R. Tsunoda, Computations of local ion energy balance in the auroral zone, *J. Geophys. Res.*, *98*, 15667-15676, 1993.

Smith, R. W., D. Rees, and R. D. Stewart, Southern hemisphere thermospheric dynamics: A review, *Rev. Geophys.*,*26*, 591-622, 1988.

Smith, R. W., J. W. Meriwether Jr., G. Hernandez, D. Rees, V. Wickwar, O. de la Beaujardiere, and T. L. Killeen, Mapping the wind in the polar thermosphere: A case study within the CEDAR program (abstract), *Eos Trans. AGU*,*70*, 161, 1989.

Smith, R. W., G. Hernandez, K. Price, G. Fraser, K. C. Clark, W. J. Schulz, S. Smith, and M. Clark, The June 1991 thermospheric storm observed in the southern hemisphere, *J. Geophys. Res.*,*99*, 17609-17615, 1994.

Spencer, N. W., L. E. Wharton, G. R. Carnigan, and J. C. Maurer, Thermosphere zonal winds, vertical motions and temperature as measured from dynamics explorer, *Geophys. Res. Lett.*,*9*, 953-956, 1982.

St. Maurice, J. P., and R. W. Schunk, Ion-neutral momentum coupling near discrete high-latitude ionospheric features, *J. Geophys. Res.*,*86*, 11299-11321, 1981.

Thayer, J. P., J. F. Vickrey, R. A. Heelis, and J. B. Gary, Interpretation and modeling of the high-latitude electromagnetic energy flux, *J. Geophys. Res.*, *100*, 19715-19728, 1995.

Walterscheid, R. L., and D. J. Boucher Jr., A simple model of the transient response of the thermosphere to impulsive forcing, *J. Atmos. Sci.*,*41*, 1062-1072, 1984.

Walterscheid, R. L., and L. R. Lyons, The neutral circulation in the vicinity of a stable auroral arc, *J. Geophys. Res.*,*97*, 19489-19499, 1992.

Walterscheid, R. L., L. R. Lyons, and K. E. Taylor, The perturbed neutral circulation in the vicinity of a symmetric stable auroral arc, *J. Geophys. Res.*,*90*, 12235-12248, 1985.

Wardill, P., and F. Jacka, Vertical motions in the thermosphere over Mawson, Antarctica, *J. Atmos. Terr. Phys.*,*48*, 289-292, 1986.

Weimer, D. R., Models of high-latitude electric potentials derived with a least error fit of spherical harmonic coefficients, *J. Geophys. Res.*,*100*, 19595-19607, 1995.

Wickwar, V. B., J. W. Meriwether, P. B. Hays, and A. F. Nagy, The meridional thermospheric neutral wind measured by radar and optical techniques in the auroral region, *J. Geophys. Res.*,*89*, 10987-10998, 1984.

Wilksch, P. A., Instrument function of the Fabry-Perot spectrometer, *Appl. Opt.*,*24*, 1502-1511, 1985.

M. Conde and R. W. Smith, Geophysical Institute, University of Alaska, 903 Koyukuk Drive, PO Box 757320, Fairbanks, AK, 99775-7320, (e-mail: conde@giuaf.gi.alaska.edu)

(Received June 30, 1997; revised October 14, 1997; accepted November 12, 1997.)